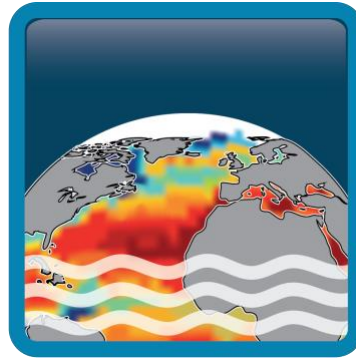


Climate Change Initiative+ (CCI+) Phase 2

Sea Surface Salinity



[D2.3] End-to-End ECV Uncertainty Budget (E3UB)

Customer: ESA

Ref.: ESA-EOP-SC-AMT-2021-26

Version: v5.0

Ref. internal: 4000123663/18/I-NB_v5r0




Revision Date: 14/10/2024

Filename: SSS_cci-D2.3-E3UB-v5r0_fbsaved0_jb

Deliverable code: D2.3



Signatures

| | | | |
|-------------|---|--|------------|
| Author | Jean Luc Vergely Fabrice Bonjean |  | 15-11-2024 |
| Reviewed by | Jacqueline Boutin (Science Leader) | | |
| | | | |
| | | | |
| | | | |
| Approved By | Jacqueline Boutin (Science Leader) |  | 15-11-2024 |
| | Nicolas Reul (Science Leader) | | |
| | Rafael Catany (Project Manager) |  | 15-11-2024 |
| Accepted by | Susanne Mecklenburg (Technical Officer) ESA | | |

| |
|--|
| Diffusion List |
| Sea Surface Salinity Team Members |
| ESA (Susanne Mecklenburg, Roberto Sabia) |

Amendment Record Sheet

| DATE / ISSUE | DESCRIPTION | SECTION / PAGE |
|-----------------------------------|--|-----------------------------|
| 15-07-2019 / v1.0 | Delivery to ESA | New document |
| 21-10-2019 / v1.1 | Update reference document documents section | Section 1.3.2 / page 14 |
| | Implemented description of the sensors mounted in each satellite | Section 2 / page 21 – 22 |
| | Added overview about PiMEP | Section 4.4.2 / page 31 |
| | Added definition PCTVAR | Section 5.3.1 / page 63 |
| | Improved Figure 33. Now all markers are visible as described in figure caption. | Section 5.3.2 / page 65 |
| 19/12/2019 / v1.2 | Edited description about PiMEP | Section 4.4.2 / page 31 |
| 19/12/2019 / v1.2 | Added band width of Aquarius satellite is 25 MHz | Section 2.4 / page 22 |
| 19/12/2019 / v1.2 | Added clarification text about Figure 32, stating that further analyses is needed and it will be provided in next version of the document. | Section 5.2.2 / page 60 |
| 19/12/2019 / v1.2 | Edited caption Figure 34. Now the caption read “2016-2018” as seen in the main text too. | Section 5.3.2 / page 63 |
| 08-07-2020 / v2.1 | Document update for delivery MS#04 to ESA | Version 2.1 of the document |
| 10-11-2020 / v2.2 | Implement ESA’s feedback (minor changes) | N/A |
| 13-09-2021 / v3.1 (this document) | Phase 1 final version | All |
| 02-05-2023 / v4.0 (this document) | Phase 2 v4 draft | All |
| 15-11-2024 /v5.0 (this document) | Phase 2 v5 draft | All |



Table of Contents

| | | |
|-----------|---|-----------|
| 1 | Introduction | 12 |
| 1.1 | Scope of this document | 12 |
| 1.2 | Structure of the document | 12 |
| 1.3 | References | 12 |
| 1.3.1 | Applicable Documents | 12 |
| 1.3.2 | Reference Documents | 13 |
| 1.4 | Acronyms | 15 |
| 2 | Sensor main characteristics..... | 18 |
| 2.1 | Introduction..... | 18 |
| 2.2 | SMOS..... | 18 |
| 2.3 | SMAP..... | 18 |
| 2.4 | Aquarius | 19 |
| 3 | L1 uncertainty characterisation..... | 20 |
| 3.1 | Introduction..... | 20 |
| 3.2 | SMOS sensor..... | 20 |
| 3.3 | SMAP and Aquarius sensors | 21 |
| 3.4 | RFI filtering | 21 |
| 4 | L2OS uncertainty characterisation | 23 |
| 4.1 | Introduction..... | 23 |
| 4.2 | Methods | 23 |
| 4.2.1 | Random uncertainty | 23 |
| 4.2.1.1 | Introduction | 23 |
| 4.2.1.2 | Random uncertainty propagation..... | 23 |
| 4.2.1.3 | Random uncertainty from the external data comparison..... | 24 |
| 4.2.1.4 | Random uncertainty from self-consistency analysis | 24 |
| 4.2.1.5 | Qualitative estimation of random uncertainty and identification of outliers | 25 |
| 4.2.2 | Systematic uncertainty | 25 |
| 4.2.2.1 | Introduction | 25 |
| 4.2.2.2 | Relative systematic uncertainties | 25 |
| 4.2.2.3 | Absolute systematic uncertainties..... | 27 |
| 4.2.2.4 | Systematic uncertainties due to TB modelling | 27 |
| 4.2.2.4.1 | Systematic uncertainties due to RFI..... | 28 |
| 4.2.2.4.2 | General approach..... | 28 |
| 4.2.2.4.3 | Method and algorithm | 29 |
| 4.3 | Uncertainty estimates of SMOS, SMAP and Aquarius SSS. | 30 |
| 4.3.1 | Introduction..... | 30 |
| 4.3.2 | External data..... | 30 |



| | | |
|-------------|--|-----------|
| 4.3.2.1 | PI-MEP (from https://www.smos-pimep.org/overview.html) | 30 |
| 4.3.2.2 | ISAS..... | 31 |
| 4.3.3 | Data analysis..... | 32 |
| 4.3.3.1 | Introduction | 32 |
| 4.3.3.2 | SMOS L2OS data..... | 33 |
| 4.3.3.2.1 | Random uncertainty..... | 34 |
| 4.3.3.2.1.1 | Random uncertainty propagated in the L2OS processor | 34 |
| 4.3.3.2.1.2 | Random uncertainty estimated by using an empirical approach..... | 35 |
| 4.3.3.2.2 | Systematic uncertainty..... | 37 |
| 4.3.3.2.2.1 | Characterisation of systematic uncertainties related to rainfall events | 37 |
| 4.3.3.2.2.2 | Characterisation of systematic uncertainties related to the dielectric constant 41 | |
| 4.3.3.2.2.3 | Characterisation of systematic uncertainties related to wind speed..... | 41 |
| 4.3.3.2.2.4 | Characterisation of latitudinal seasonal systematic uncertainties..... | 45 |
| 4.3.3.2.2.5 | Characterisation of RFI systematic uncertainties: A Prototype Example of the RM Method. 48 | |
| 4.3.3.2.3 | flagging the data..... | 55 |
| 4.3.3.3 | SMAP L2 data | 56 |
| 4.3.3.4 | Random uncertainty..... | 56 |
| 4.3.3.4.1 | Systematic uncertainty..... | 57 |
| 4.3.3.4.1.1 | Characterization of systematic uncertainties related to the dielectric constant 57 | |
| 4.3.3.4.1.2 | Characterisation of latitudinal seasonal systematic uncertainties..... | 58 |
| 4.3.3.4.2 | flagging the data..... | 60 |
| 4.3.3.5 | Aquarius L3 data | 60 |
| 4.3.3.6 | Random uncertainty..... | 60 |
| 4.3.3.7 | Systematic uncertainty..... | 61 |
| 4.3.3.7.1.1 | Characterisation of systematic uncertainties related to the dielectric constant 61 | |
| 4.3.3.7.1.2 | Characterisation of latitudinal seasonal systematic uncertainties..... | 63 |
| 4.3.3.7.2 | flagging the data..... | 64 |
| 5 | <i>L3 and L4 uncertainty budget.....</i> | 65 |
| 6 | <i>Conclusions and the way forward</i> | 66 |



List of figures

Figure 1: Histogram of the new random variable X (reduced centred SSS) after applying a coastal correction. Top: pixels near the coast ($d_{\text{coast}} < 400$ km); bottom: pixels in the open ocean.

Figure 2: uncertainty factor according to the distance to the coast.----- 36

Figure 3: Corrected SSS – ISAS SSS with different W_{Smin} cutoffs in case of heavy rain and high SST ($>25^{\circ}\text{C}$). Top left, W_{S} -independent $a_0(\text{RR})$ correction; then, from top to bottom and from left to right, W_{Smin} cutoff taken at 1, 2, 3, 4, 5 m/s respectively. Median and std differences are reported in the title of the figures for each W_{Smin} cutoff.----- 38

Figure 4. Top: median(SMOS-ISAS) as a function of the W_{Smin} parameter chosen as cut-off. Bottom: std(SMOS-ISAS). ----- 39

Figure 5: idem Figure 3 with an SST between 10 and 20°C ----- 39

Figure 6: idem Figure 4 with an SST between 10 and 20°C ----- 40

Figure 7: correction of the effect of rain on SSS according to various W_{S} . The correction integrated overall wind speeds is shown as a blue curve. ----- 41

Figure 8: Number of flags raised as a function of time for the 6 L2OS classes from ERA5 model 43

Figure 10: SSS biases in the (W_{S} ,SST) plane (descending orbits). Left: roughness dominated by the swell; right: roughness dominated by the wind sea.----- 44

Figure 11: Correction at 15°C for the 3 SSS (uncorr, corr and acard) and the two sea classes (swell and wind). ----- 44

Figure 12: Mask for seasonal latitudinal correction ----- 46

Figure 13: example of latitudinal correction for the 2 SMOS SSS ($\text{SSS}_{\text{uncorr}}$ on the left and $\text{SSS}_{\text{acard}}$ on the right). Ascending dwells are shown on the left-hand side of each figure, descending dwells on the right-hand side. Month of June. The y-axis gives the distance from the track in km. ----- 47

Figure 14: Hovmoller of the difference between $\text{SSS}_{\text{uncorr}}$ and ISAS, ascending orbits. Left: before latitudinal correction; right: after latitudinal correction. Top, CCIv4; bottom, CCIv5. ----- 47

Figure 15: idem than Figure 14 for descending orbits. ----- 48

Figure 20: (Top) Monthly global map including swath interval $[+137.5\text{km}, +162.5\text{km}]$ of SSS for all descending half orbits in August 2017. (Bottom) Zoom in over the Samoa region for $[+112.5\text{km}, +137.5\text{km}]$, $[+137.5\text{km}, +162.5\text{km}]$, $[+162.5\text{km}, +187.5\text{km}]$ intervals of descending half orbits for the same month. ----- 49

Figure 21: Examples of swath-interval differences calculated from the 11-month moving averaged SSS swath intervals. (Left) Maps of the std over the entire period of the absolute difference of various 11-



month m.a. swath-interval fields. (Right) Angular hovmöller plots where directions E, NE, ... are indicated in the rose around the source (P1) on the Left and where SSS is averaged over the angular sectors diverging from the source. ----- 50

Figure 22: 1st mode results of the PCA applied to the dwell-line differences. (Top-Left) Percentage of variance explained by the PCA modes as a function of the mode number. (Top-Bottom) Spatial structures of the first mode are given in angular sectors around the RFI source. (Right) The time series is associated with the first mode (in pss). ----- 51

Figure 23: Portion of the spatial patterns related to the initial regression utilized to compute $V0'(dk, x, y)$, which is the spatial element of the correction package. ----- 52

Figure 24: (Blue) Monthly RFI characteristic time series $U01(t)$ obtained by projecting the monthly dwell-line agglomerates onto the RFI spatial structures. (Orange) The (11-month m.a.) characteristic time series previously calculated is superimposed for comparison. ----- 52

Figure 25: Example of correction for a specific dwell line (Ascending, -237.5km,-212.5km) in July 2012. (Left) Initial dwell field SSS anomaly (with respect to time mean). (Middle) Corrected dwell field anomaly. (Right) Difference between corrected and initial fields. ----- 53

Figure 26: Performance of the correction method with respect to ISAS-20 5m salinity. Here we average SSS over all the dwell lines, add a constant time-mean field, and look at angular hovmoller variations around the source (Left) All-dwell mean of initial SSS. (Middle) All-dwell mean of corrected SSS. (Right) ISAS20 5m salinity. ----- 53

Figure 27: Performance of the correction method with respect to ISAS-20 5m salinity. Here we calculate and plot a performance metric with respect to ISAS20 at each grid point. All dwell SSS are preliminarily averaged. (Left) Plot of the metric $std(sat - isas)/std(isas)$, for the initial SSS dwell data. (Middle) Plot of the same metric for the corrected SSS dwell data. (Right) Difference (Middle)-(Left), that highlights improvement (blue) or degradation (red) with respect to ISAS20. ----- 53

Figure 23: Left and Center Columns: Std of the difference between gridded SMOS and ISAS20 datasets before and after RFI correction, $std(SMOS - ISAS)$. Right Column: Difference between the maps in the left and center columns, $std(SMOS \text{ before correction} - ISAS) - std(SMOS \text{ after correction} - ISAS)$, representing a performance metric. Positive values (blue) indicate improvement, while negative values (red) indicate degradation. Each row corresponds to a specific region: Top – Samoa, Middle – Barbados, Bottom – Guinea Gulf.----- 54

Figure 24: Same as the right column of Figure 23, but applied to the entire ocean domain, from 70°S to 70°N. ----- 55

Figure 28: SSS SMAP uncertainty obtained by comparing aft and fore acquisitions.----- 57

Figure 29: uncertainty factor according to the distance to the coast. SMAP.----- 57

Figure 30. Left: SSS bias in the (SSS,SST) plan. Fore acquisition, A orbits. Right: average bias according to SST. In green, the average relation for the corrections. SMAP. ----- 58



Figure 26: Seasonal latitudinal correction for SMAP. Fore acquisition, ascending orbits. ----- 58

Figure 33: SMAP-ISAS after SST and latitudinal fore acquisition correction. Left: ascending orbits; right: descending orbits. Uncorrected inter-annual biases are observed in descending orbits, from beginning of 2013. Top: SMAPv5.0; bottom: SMAPv5.3. ----- 59

Figure 34: idem Figure 33 for afte acquisition.----- 59

Figure 39: SSS Aquarius uncertainty obtained by comparing 7 day acquisitions. ----- 61

Figure 40: uncertainty factor according to the distance to the coast. Aquarius. ----- 61

Figure 41: Example of the Aquarius bias for January (climatology) to be compared with the SST field. The positive SSS anomaly in the Southeastern Atlantic Ocean and Indian Ocean is correlated with a northern SST front. ----- 62

Figure 42. Left: Aquarius bias in the (SSS,SST) plan. Right: bias as a function of SST. In green, the average relationship for the corrections; in blue, the relationship obtained with ascending orbits and in red, with descending orbits.----- 62

Figure 43: Aquarius-ISAS differences over 2013-2014. Left, uncorrected for SST; right, corrected for SST. Ascending orbits. ----- 63

Figure 44: Hovmöller of the Aquarius-ISAS difference. Left, uncorrected for SST; right, corrected for SST. Ascending orbits. ----- 63

Figure 45: Latitudinal correction applied for Aquarius as a function of month and latitude. This correction is given at an average SST. Left, ascending orbits, right, descending orbits. ----- 64

Figure 46: Hovmöller of SSS Aquarius - SSS ISAS. SSS Aquarius corrected for SST-dependent bias and latitudinal seasonal bias. Left, ascending orbits; right, descending orbits. ----- 64



***Climate Change Initiative+ (CCI+)
Phase 2***

End-to-End ECV Uncertainty Budget

Ref.: ESA-EOP-SC-AMT-2021-26

Date: 15/11/2024

Version: v5.0

Page: 11 of 67

List of tables

Table 1: L2OS sea states -----42



1 Introduction

1.1 Scope of this document

This document holds the End-to-End ECV Uncertainty Budget (E3UB) prepared by the CCI+ Salinity team (CRDPv5).

At the moment of writing this report, SSS measurements are available from three L-Band radiometer satellite missions, SMOS, Aquarius and SMAP, each with very different instrument features leading to particular measurement characteristics. The Climate Change Initiative Salinity project (CCI+SSS) aimed to produce SSS Climate Data Record (CDR) to include satellite measurements and well-documented uncertainties. In order to ensure a consistent CDR, variations in instruments are closely examined by comparing SSS data and then adjusted using a thorough analysis of the satellite measurements and outside referral sources. This document describes the basis for the uncertainties characterisations.

1.2 Structure of the document

The E3UB is structured as follows:

This document is composed of 4 major sections:

- ✓ Section 2: Sensor main characteristics
- ✓ Section 3: L1 uncertainty characterisation
- ✓ Section 4: L2 uncertainty characterisation
- ✓ Section 5: L3 and L4 uncertainty budget

L2/L3/L4 data sets will be provided in parts 1 and 2 of the CCI+SSS phase 2 project and are described in the SRD.

This document is the fifth version of the E3UB document addressing Phase 2, part 2 activity.

1.3 References

1.3.1 Applicable Documents

| ID | Document | Reference |
|------|---|--------------------------|
| AD01 | CCI+ Statement of Work | SoW |
| AD02 | Product User Guide (PUG) | SSS_cci-D4.3-PUG-v3.0 |
| AD03 | User Requirement Document (URD) | SSS_cci-D1.1-URD-v3 |
| AD04 | Product Specification Document (PSD) | SSS_cci-D1.2-PSD-v3 |
| AD05 | Algorithm Theoretical Baseline Document | SSS_cci-D2.3-ATBD_L3_L4- |



**Climate Change Initiative+ (CCI+)
Phase 2**

End-to-End ECV Uncertainty Budget

Ref.: ESA-EOP-SC-AMT-2021-26

Date: 15/11/2024

Version: v5.0

Page: 13 of 67

| ID | Document | Reference |
|-------------|---|-----------------------------------|
| AD06 | End-to-End ECV Uncertainty Budget (E3UB), version 1 | SSS_cci-D2.3-E3UB_v3 |
| AD07 | Algorithm Theoretical Baseline Document, version 2 | SSS_cci-D2.3-ATBD_v4 |
| AD08 | End-to-End ECV Uncertainty Budget (E3UB), version 2 | SSS_cci-D2.3-ATBD_L3_L4-i1r0_v2 |
| AD09 | Algorithm Theoretical Baseline Document, version 3 | SSS_cci-D2.3-ATBD_L3_L4-i1r0_v3.0 |
| AD10 | Algorithm Theoretical Baseline Document, version 4 | SSS_cci-D2.3-ATBD_L3_L4-i1r0_v4.0 |

1.3.2 Reference Documents

| ID | Document | Reference |
|-------------|---|-----------------------------|
| RD01 | Boutin, J., N. Martin, N. Kolodziejczyk, and G. Reverdin (2016a), Interannual anomalies of SMOS sea surface salinity, <i>Remote Sensing of Environment</i> , doi:http://dx.doi.org/10.1016/j.rse.2016.02.053 | |
| RD02 | Kolodziejczyk, N., J. Boutin, J.-L. Vergely, S. Marchand, N. Martin, and G. Reverdin (2016), Mitigation of systematic errors in SMOS sea surface salinity, <i>Remote Sensing of Environment</i> , doi:http://dx.doi.org/10.1016/j.rse.2016.02.061. | |
| RD03 | Evaluation of measurement data – Guide to the expression of uncertainty in measurement, JCGM 100:2008 | |
| RD04 | SMOS ATBD L2OS v3.13, 29 April 2016 | SO-TN-ARG-GS-0007 |
| RD05 | AQ-014-PS-0017_Aquarius_L2toL3ATBD_DatasetVersion5.0 Liang Hong, Normal Kuring, Joel Gales and Fred Patt | |
| RD06 | AQ-014-PS-0018_AquariusLevel2specification_DatasetVersion5.0 Fred Patt, Liang Hong | |
| RD07 | SMAP_RemSSS_Release_V2.0 | |
| RD08 | Meissner, T. and F. J. Wentz, 2016: Remote Sensing Systems SMAP Ocean Surface Salinities [Level 2C, Level 3 Running 8-day, Level 3 Monthly], Version 2.0 validated release. Remote Sensing Systems, Santa Rosa, CA, USA. Available online at www.remss.com/missions/smap, doi: 10.5067/SMP20-2SOCS (L2C files). | |
| RD09 | Boutin J., J.-L. Vergely, S. Marchand, F. D'Amico, A. Hasson, N. Kolodziejczyk, N. Reul, G. Reverdin, J. Vialard (2018), New SMOS Sea Surface Salinity with reduced systematic errors and improved variability, <i>Remote Sensing Of Environment</i> , doi:http://dx.doi.org/10.1016/j.rse.2018.05.022 | |
| RD10 | Thomas Meissner + Frank Wentz Remote Sensing Systems, Santa Rosa, CA, RSS SMAP Salinity: Version 2 Validated Release. Algorithm Theoretical Basis Document (ATBD), September 13, 2016 | RSS Technical Report 091316 |
| RD11 | Dinnat, E., D. Le Vine, J. Boutin, T. Meissner, and G. Lagerloef. 2019. "Remote Sensing of Sea Surface Salinity: Comparison of Satellite and In Situ Observations and Impact of Retrieval Parameters." <i>Remote Sensing</i> , 11 (7) : 750 | |
| RD12 | C. J. Merchant et al. (2017): Uncertainty information in climate data records from Earth observation, <i>Earth Syst. Sci. Data</i> , 9, 511-527 | |



**Climate Change Initiative+ (CCI+)
Phase 2**

End-to-End ECV Uncertainty Budget

Ref.: ESA-EOP-SC-AMT-2021-26

Date: 15/11/2024

Version: v5.0

Page: 14 of 67

| ID | Document | Reference |
|-------------|--|-----------------------------|
| RD13 | Brodzik, M. J., B. Billingsley, T. Haran, B. Raup, and M. H. Savoie (2012), EASE-Grid 2.0: Incremental but Significant Improvements for Earth-Gridded Data Sets, <i>ISPRS International Journal of Geo-Information</i> , 1(1), 32-45. | |
| RD14 | Le Vine, D. M., and P. de Mattheaïs (2014), Aquarius active/passive RFI environment at L-band, <i>IEEE Geosci. Remote Sens. Lett.</i> , 11(10), doi:10.1109/LGRS.2014.2307794. | |
| RD15 | Drushka, K., Asher, W. E., Ward, B., and Walesby, K. (2016), Understanding the formation and evolution of rain-formed fresh lenses at the ocean surface, <i>J. Geophys. Res. Oceans</i> , 121, 2673– 2689, doi:10.1002/2015JC011527. | |
| RD16 | Supply, A., J. Boutin, G. Reverdin, J.-L. Vergely, and H. Bellenger, 2020: Variability of satellite sea surface salinity under rainfall. In: <i>Satellite Precipitation Measurement</i> , V. Levizzani, C. Kidd., D. B. Kirschbaum, C. D. Kummerow, K. Nakamura, F. J. Turk, Eds., Springer Nature, Cham, <i>Advances in Global Change Research</i> , 69, 1155-1176, https://doi.org/10.1007/978-3-030-35798-6_34 . | |
| RD17 | Boutin, J., J.L. Vergely, F. Bonjean, X. Perrot, Y. Zhou, E. Dinnat, R. Lang, D. Levine, and R. Sabia, New Seawater Dielectric Constant Parametrization and Application to SMOS Retrieved Salinity, <i>IEEE Transactions of Geoscience and Remote Sensing</i> , 2023, doi : 10.1109/TGRS.2023.3257923. | |
| RD18 | Thomas Meissner + Frank Wentz Remote Sensing Systems, Santa Rosa, CA, RSS SMAP Salinity: Version 6.0 Validated Release. Algorithm Theoretical Basis Document (ATBD), January 18, 2024 | RSS Technical Report 011824 |
| RD19 | F. Bonjean, J. Boutin, J. -L. Vergely, P. Richaume and R. Sabia, "Recovery of SMOS Salinity Variability in RFI-Contaminated Regions," in <i>IEEE Transactions on Geoscience and Remote Sensing</i> , vol. 62, pp. 1-19, 2024, Art no. 5301619, doi: 10.1109/TGRS.2024.3408049. | |



1.4 Acronyms

| | |
|--------|---|
| AD | Applicable document |
| ADB | Actions database |
| AMOC | Atlantic Meridional Overturning Circulation |
| ATBD | Algorithm theoretical basis documents |
| BRO | Brochure |
| CliC | Climate and Cryosphere |
| DIR | Directory |
| DS | Dataset availability |
| DS-UM | Dataset user manual |
| DVP | Development and validation plan |
| EC RTD | European Commission Directorate General for Research and Innovation |
| EDS | Experimental dataset |
| EMI | Electromagnetic Interference |
| EO | Earth Observation |
| EOEP | Earth Observation Envelope Program |
| ESA | European Space Agency |
| FR | Final review |
| FWF | Freshwater fluxes |
| GCOS | Global Climate Observing System |
| IAR | Impact assessment report |
| ITT | Invitation to tender |
| IPP | Year of Polar Prediction |
| KO | Kick-off |
| MR | Monthly report |
| MTR | Mid-term review |
| MV-TN | Modelling and validation technical note |
| NDVI | Normalised Difference Vegetation Index |
| OTT | Ocean Target Transform |
| PAR | Preliminary analysis report |
| PGICs | Peripheral glaciers and ice caps |
| PM | Progress meeting |
| PMP | Project management plan |
| RD | Reference document |
| RB | Requirements baseline |
| SAR | Synthetic Aperture Radar |
| SIAR | Scientific and impact assessment report |



**Climate Change Initiative+ (CCI+)
Phase 2**

End-to-End ECV Uncertainty Budget

Ref.: ESA-EOP-SC-AMT-2021-26

Date: 15/11/2024

Version: v5.0

Page: 16 of 67

| | |
|--------|---|
| SMAP | Soil Moisture Active Passive |
| SMOS | Soil Moisture and Ocean Salinity |
| SoW | Statement of work |
| SR | Scientific roadmap |
| SSS | Sea Surface Salinity |
| SST | Sea Surface Temperature |
| TDP | Technical data package |
| TDS | Training Data Set |
| TN | Technical note |
| VIR | Validation and intercomparison report |
| VR | Validation report |
| WCRP | World Climate Research Programme |
| WP | Work package |
| WS | Wind Speed |
| WWRP | World Weather Research Programme |
| AD | Applicable document |
| ADB | Actions database |
| AMOC | Atlantic Meridional Overturning Circulation |
| ATBD | Algorithm theoretical basis documents |
| BRO | Brochure |
| BV | Boutin-Vergely dielectric constant model |
| BVZ | Boutin-Vergely-Zhou dielectric constant model (RD17) |
| CliC | Climate and Cryosphere |
| DIR | Directory |
| DS | Dataset availability |
| DS-UM | Dataset user manual |
| DVP | Development and validation plan |
| EC RTD | European Commission Directorate General for Research and Innovation |
| EDS | Experimental dataset |
| EMI | Electromagnetic Interference |
| EO | Earth Observation |
| EOEP | Earth Observation Envelope Program |
| ESA | European Space Agency |
| FR | Final review |
| FWF | Freshwater fluxes |
| GCOS | Global Climate Observing System |
| IAR | Impact assessment report |



**Climate Change Initiative+ (CCI+)
Phase 2**

End-to-End ECV Uncertainty Budget

Ref.: ESA-EOP-SC-AMT-2021-26

Date: 15/11/2024

Version: v5.0

Page: 17 of 67

| | |
|-------|---|
| ITT | Invitation to tender |
| IPP | Year of Polar Prediction |
| KO | Kick-off |
| KS | Klein and Swift dielectric constant model |
| MR | Monthly report |
| MTR | Mid-term review |
| MV-TN | Modelling and validation technical note |
| NDVI | Normalised Difference Vegetation Index |
| PAR | Preliminary analysis report |
| RFI | Radio-Frequency Interference |
| TB | Brightness Temperature |



2 Sensor main characteristics

2.1 Introduction

This section presents the main characteristics of SMOS, SMAP and Aquarius sensors. It provides information about revisit time and mean footprint resolution.

2.2 SMOS

The main SMOS characteristics are:

- ✓ Interferometric radiometer with a centre frequency of 1.41 GHz and bandwidth of 27 MHz
- ✓ Data time coverage: 2010-now
- ✓ sub-cycle of 18 days
- ✓ Exact repetitive cycle: 149 days
- ✓ Earth Incidence Angle: 0-60°.
- ✓ Local ascending/descending time: 6 AM/PM.
- ✓ four polarisations
- ✓ 3-dB (half power) footprint size: between ~32 and 100 km (according to the incidence angle)
- ✓ Global coverage: 3 days

2.3 SMAP

The main SMAP characteristics are:

- ✓ Radiometer (6-meter mesh antenna) with a centre frequency of 1.41 GHz and bandwidth of 24 MHz
- ✓ Exact repetitive cycle of 8 days
- ✓ aft and fore acquisition
- ✓ Data time coverage: 04/2015 to now
- ✓ Conical scanning at 14.6 rpm. Scan time: 4.1 sec
- ✓ Earth Incidence Angle: 40°.
- ✓ Local ascending/descending time: 6 PM/AM.
- ✓ four polarisations
- ✓ 1000 km wide swath.



- ✓ 3-dB (half power) footprint size: ~43 km.
- ✓ Global coverage: 3 days

2.4 Aquarius

The main Aquarius characteristics are:

- ✓ Radiometer (3 beams) with a centre frequency of 1.413 GHz and bandwidth of 25 MHz.
- ✓ Exact repeat cycle of 8 days
- ✓ Almost global coverage: 7 days
- ✓ Data time coverage: 08/2011 to 06/2015.
- ✓ Earth incidence angles: 28.7, 37.8, and 45.6°.
- ✓ Footprints for the beams are 74 km along track x 94 km cross track, 84x120 km and 96x156 km yielding a total cross-track of 390 km.
- ✓ Measurement every 1.44s (about every 10 km).
- ✓ Distance between beam swaths of about 100 and 150 km (across-track).
- ✓ Local ascending/descending time: 6 PM/AM.
- ✓ TH, TV and third Stokes
- ✓ Aligned with a scatterometer (1.26 GHz), both instruments are polarimetric.



3 L1 uncertainty characterisation

3.1 Introduction

In order to better understand the SSS uncertainties at L4, we need to have a global understanding of what happens at L0-L1 in terms of the TB uncertainty budget. L0-L1 processings are very complex and require specific expertise. Indeed, reviewing all L0-L1 processing methods for all satellite missions is outside our scope. Our purpose is to replay L2 from existing L1 products. Therefore, it is not our objective to re-estimate TB uncertainties but to take what comes out of the L0-L1 products and work with them, as long as we have sufficient information to propagate TB uncertainties toward level 2 properly. TBs at the L1 processing output have systematic uncertainties that are not corrected at L0-L1 and that we take into account in the higher levels empirically.

Hence, we develop methods for correcting systematic uncertainties and estimating random uncertainties at the SSS level from the remaining differences between forward model predictions and TB data from SMOS, Aquarius or SMAP. Seasonal patterns of these differences can vary from ascending to descending passes. This is mainly due to uncertainties in the thermal model and instrument monitoring, inaccurate Radiative Transfer Models (RTMs), and input auxiliary EO data.

3.2 SMOS sensor

SMOS is an L-band interferometer that measures the Fourier transform of the scene. Level 1 processing is the passage of visibilities (which integrate antenna gains) to the Fourier transform of TB, then the passage of TB in the frequency space domain to the physical space domain. This different processing requires knowledge of antenna gains, with, as an additional difficulty, a spatial sampling of the observed frequencies lower than Shannon's sampling. Since the scene has infinite frequencies, this poses specific difficulties for the passage into the physical space domain. In the following this operation is called reconstruction

Complex calibrations for thermal drifts based on Noise Injection Radiometer data and several onboard thermistor measurements are used to calibrate the visibilities. Short-term calibration is regularly performed raw to compensate for high variability drifts. In addition, cold-sky calibration is performed several times a year when the satellite sensor is rotated sky upward during dedicated manoeuvres (used for the so-called Flat Target Transformation). However, systematic and seasonal image reconstruction uncertainties are still found in the reconstructed level 1 data despite raw data calibration. This can occur, for example, due to the instrument's response to a very strong L-band source in the field of view, such as the sun image and its tails corrupting the quality of the reconstructed brightness, but also because of image reconstruction systematic uncertainties (noise floor, aliasing, instrument impulse response function, antenna pattern uncertainties).

To compensate for these distortions in the image, a vicarious calibration is performed. This involves comparing the SMOS antenna TBs with a radiative transfer forward model of the



brightness obtained from specific orbits in the middle of the Pacific and evaluating the mean spatial difference in the antenna coordinate frame. The forward model is derived using climatology of SSS or analysed in situ data (ISAS fields) interpolated along the half-orbits used for calibration. The Tb adjustment is named the Ocean Target Transformation (OTT).

Following this correction, it is possible to empirically validate the uncertainties on TBs against the expected radiometric noise. These uncertainties result from filtering out various unmodeled contributions, such as RFI and sun effect, which align with the expected radiometric noise. On the other hand, there are reconstruction biases that are not corrected by the OTT, which then generates biases in the estimated parameters. For now, L1 processing does not make it possible to avoid such biases.

3.3 SMAP and Aquarius sensors

To correct for residual drifts after raw data calibration, NASA algorithms thus use the median difference between Aquarius (or SMAP) data and forward radiative transfer model simulations of the brightness temperature obtained by using HYCOM model SSS or Argo SSS (depending on the release) as a forcing parameter. The difference is then averaged globally, and the mean difference evaluated daily is used for post-calibration adjustments.

For SMAP (it is more complicated than Aquarius: the SMAP antenna has some non-negligible emissivity), the antenna temperature predicted from the thermal model has some uncertainties, and a latitudinal correction has to be applied.

In addition, uncertainties in the modelled side-lobes of the radiometer antenna patterns used for antenna temperature provide some signal leakage of the brighter sources (land, sea ice) into the lighter source (pure ocean). These so-called "land contamination" or "ice contamination" need to be corrected for the input TB to retrieve an unbiased SSS as close as possible from the coastlines or ice edges. A method of contrasting half-space is currently used in NASA algorithms to adjust antenna pattern corrections when Aquarius or SMAP pass through two sharply contrasted (in the TB sense) semi-infinite surfaces (from sea to land, for instance).

3.4 RFI filtering

SMOS, Aquarius, and SMAP missions operate in the L-band protected spectrum (1400-1427 MHz), which is nevertheless now known to be vulnerable to radio-frequency interference (RFI). Areas affected by RFI might experience data loss or result in inaccurate soil moisture and ocean salinity retrieved values. Several strategies were implemented to filter data from RFI contaminated measurements to alleviate this situation. As SMOS, launched in 2009, was the first satellite to operate in L-band, it does not have any onboard hardware/software to filter RFI, so RFI filtering/mitigation relies only on data post-acquisition processing. This issue is significantly less critical for SMAP (and to the least extent for Aquarius), as they are (were) equipped with onboard frequency/time-domain-based RFI filters.



*Climate Change Initiative+ (CCI+)
Phase 2*

End-to-End ECV Uncertainty Budget

Ref.: ESA-EOP-SC-AMT-2021-26

Date: 15/11/2024

Version: v5.0

Page: 22 of 67

Over the ocean, SMOS data are contaminated by RFI emitted principally from land. The impact on the reconstructed brightness temperature can be positive or negative and is not limited to the location of the on-ground antenna causing the interference but affects measurements as soon as there is a line of sight between the instrument and the RFI source (Corbella, Martín-Neira, Oliva, Torres, & Duffo, 2012). Due to the interferometer principle from a Y-shape antenna, the contamination is not circular symmetric in SMOS images but presents six prominent tails spreading from the RFI source. In the case of SMAP and Aquarius, the RFI contamination is different as they operate real-aperture radiometers and onboard data filtering with enhanced detection capabilities. To protect against RFI, Aquarius employs rapid sampling (10 ms, milliseconds) and a "glitch" detection algorithm that looks for outliers among the samples. Samples identified as RFI are removed, and the remainder is averaged to produce an RFI-free signal for the salinity retrieval algorithm. The RFI detection algorithm works well over the ocean with modest rates for false alarms (5%) and missed detection. However, RFI is still detected in Aquarius (Le Vine and De Matthaeis, 2014). SMAP takes a multidomain approach to RFI mitigation by utilising an innovative onboard digital detector back end with digital signal processing algorithms to characterise the received signals' time, frequency, polarization, and statistical properties. Almost 1000 times more measurements than conventionally necessary are collected to enable the ground processing algorithm to detect and remove interferences.



4 L2OS uncertainty characterisation

4.1 Introduction

SSS random uncertainties are taken directly from L2 products (L2 random theoretical uncertainties), estimated from self-consistency analysis, or by adjusting global metrics of differences between observed SSS with external data (ISAS, Argo). Random and systematic uncertainties can be obtained in a relative way by comparing averaged products from different sensors and orbit types (ascending or descending).

L2 SSS random uncertainty is first derived for open ocean data. In the second step, their estimate is updated in case of land contamination. We extract from L2 data a multiplicative factor to be applied to the SSS random uncertainties. This factor allows taking into account secondary side lobe effects or reconstruction effects affecting TB measurements close to the coast.

In the following, we present the generic methods in section 4.2 and the uncertainty estimates obtained with version 5 of the CCI+SSS processing in section 4.3.

4.2 Methods

4.2.1 Random uncertainty

4.2.1.1 Introduction

In this section, we present three different methods which allow estimating SSS random uncertainties:

- by error propagation
- by comparing measured SSS with a reference (affected by a neglectable error)
- by self-consistency analysis

4.2.1.2 Random uncertainty propagation

The fundamental random uncertainties on salinity correspond to that provided in salinity level 2 products.

Level 2 algorithms are used to propagate the TB noise characterised by the radiometric accuracy and the uncertainty of all geophysical parameters (wind speed, surface temperature, etc.) on the salinity. The propagation methods generally assume a Gaussian statistic, a linearisation of the forward model near the solution and least square type retrieval. The theoretical uncertainty obtained depends on the a priori uncertainties on the parameters. In order to homogenise L2 uncertainties from the different sensors (SMOS, SMAP, Aquarius), a review of uncertainty propagation methods has been conducted. We propose a strategy to

standardise the uncertainty calculation and the a priori uncertainties assigned to the geophysical parameters. This strategy of standardising the uncertainty calculation must be in phase with the standardisation of the auxiliary data and the uniformisation of the direct and inverse models on the set of sensors. Note that for the time being, model uncertainties (sun glint, roughness, atmospheric, galactic, dielectric models) are not propagated in L2 SSS. After that, when computing L3 products by combining different L2 SSS, it is possible to use the L2 uncertainty to weight properly during the average.

The theoretical SSS a posteriori uncertainty depends on the radiometric accuracy (σ_{TB}) and the uncertainty of the auxiliary data. If these two uncertainty sources are given, the SSS uncertainty also depends mainly on the sensitivity of TB, according to the SSS. This sensitivity increases with the SST. This means that the SSS uncertainty, σ_{SSS} , increases at high latitudes. The relation is as follows:

$$\sigma_{SSS} = \sigma_{TB} \cdot \left(\frac{1}{\left| \frac{\partial TB}{\partial SSS} (SST) \right|} \right) \quad \text{Eqn 4-1}$$

This yields, according to a $\frac{\partial TB}{\partial SSS} (SST)$ approximation for Stokes1 of $-0.015 \cdot SST - 0.25$

$$\sigma_{SSS} = \frac{\sigma_{TB}}{0.015 \cdot SST + 0.25}$$

SSS uncertainties due to WS and SST uncertainties could be added quadratically to this relation after propagation.

4.2.1.3 Random uncertainty from the external data comparison

The uncertainty balance obtained by uncertainty propagation does not generally include the uncertainties on the models themselves (model of galactic noise, roughness, solar contamination, etc.). In order to estimate the errors and validate the uncertainties obtained by propagation, it is necessary to compare the satellite SSS data with external information (e.g. in-situ measurements). This can be done directly with L2 SSS. We expect the random uncertainties to decrease to zero when averaged over a large space. This is the property we use to validate the random uncertainties estimate and to discriminate it from systematic uncertainties. It is then preferable to average the L2 data before comparison in order to reduce the random uncertainty and to have an estimation of the systematic uncertainty. Hence, the external data is compared on L2 and L3 products. This approach has been performed for each sensor.

4.2.1.4 Random uncertainty from self-consistency analysis

The three sensors provide independent measurements. Three comparisons are made, depending on the period: SMOS-Aquarius over 2012-2015, SMOS-SMAP over the period 2015-2024 and SMOS-SMAP-Aquarius over April to June 2015. Note that if we standardise the direct

and auxiliary data, the random and systematic uncertainties on the SSS data will not be completely independent. On the other hand, this could make it possible to qualify uncertainties related to the unexpected behaviour of the instruments (sensor drift, issues relating to image reconstruction, contamination by RFI, etc.).

4.2.1.5 Qualitative estimation of random uncertainty and identification of outliers

In some cases, we know that estimating the random uncertainties at L2 is inaccurate (primarily if one identifies convergence problems in retrieval algorithms). In this case, it is essential to identify and flag the SSS outliers accordingly. In addition, some statistical indicators for TB residues may show that the uncertainty obtained by propagation is underestimated. It is then possible to empirically re-evaluate the SSS random uncertainties upwards.

4.2.2 Systematic uncertainty

4.2.2.1 Introduction

Estimating systematic uncertainties is much more complex than estimating random uncertainties. In fact, in most Level 2 products, the systematic uncertainty is not directly estimated. There are two types of systematic uncertainties: relative systematic differences (inter-sensor or intra-sensor) and absolute systematic uncertainties (in comparison with 'truth'). The systematic uncertainties should be corrected with identical techniques for the three sensors, this being an essential prelude before combining the data of the various sensors.

4.2.2.2 Relative systematic uncertainties

The solution to this problem is not to estimate absolute SSS but to analyse salinity anomalies. This approach has been applied to SMOS and has yielded excellent results (Boutin et al., 2016). In particular, specific algorithms allow for correcting the relative across-track systematic uncertainties (Kolodziejczyk et al. 2016) and ascending-descending latitudinal biases (Boutin et al. 2018). This type of algorithm has been extended to the other sensors in previous CCI+SSS CRDP versions (Boutin et al. 2021) and it is thus possible to estimate the relative biases for all the sensors. We recall below the principle of the method and the updates performed in CCI+SSS version 5.

Moreover, the bias also depends on the operating point and the sensitivity of TB to SSS. Some biases related to TB bias can be corrected a posteriori, for example, in relation to SST.

In order to characterise the bias, we can distinguish two types of bias:

- a land-sea contamination bias independent of time-related to the instrument function (reconstruction problem for SMOS and pollution by the existence of side lobes for SMAP and Aquarius). Even though the land emissivity is expected to vary seasonally, it is so large compared to ocean emissivity (\sim a factor 2) that, at first order, it can be considered constant.



- a seasonal latitudinal bias that depends on sun and galactic noise contamination and possibly on other instrumental drifts considered here periodic over one year. From CCI+SSS v4, this correction is applied not only on SMOS data but on other sensors.

We consider that latitudinal bias is independent of the basin (Atlantic, Pacific or Indian Ocean) and that it applies in addition to coastal bias in an additive way.

The general formulation of the bias for a given grid node at the position (lat,lon) is as follows:

$$SSS_{obs}(X, t, orb, lat, lon) = SSS(t) - bc(X, orb, lat, lon) - bl(X, orb, t_month, lat) \quad \text{Eqn 4-2}$$

With bc , coastal bias and bl latitudinal bias. SSS_{obs} is the observed salinity, and $SSS(t)$ corresponds to the unbiased SSS. X corresponds to a subset of data that is assigned in the same way through the bias. In the case of Aquarius, this may be the antenna beam or, in the case of SMOS, the position of the measurement in the swath; in the case of SMAP, the aft and fore views. As mentioned, bl is considered for Aquarius and SMAP in CCI+SSS v5 (and also in v3). For SMOS, a time-dependent correction is added in some RFI regions (see 4.2.2.4.1).

It is possible to calculate bc and bl independently starting with the calculation of bl on open sea areas taken far from the coast. Then, a latitudinal correction is applied to the coastal pixels. From these latitudinal bias-corrected data, we can estimate bc . Since the number of independent subsets of data is relatively large, the different biases can be estimated self-referenced, i.e. there is no need for an external reference when considering anomalies and not absolute salinities. Note that Eqn 4-2 requires simultaneous estimation of $SSS(t)$ (or anomalies with respect to a reference salinity given by the measurements themselves) and biases bc and bl since we do not use an external reference that gives us $SSS(t)$. This is a critical point because, in this situation, we estimate the L4 products represented by $SSS(t)$ simultaneously as we characterise the biases. The uncertainty propagation occurs at the time of this estimate. Because of this remark, an estimation method should be proposed. We have chosen to perform a Bayesian least square method that includes a time correlation length. We can process each grid node independently of each other and thus maintain the native spatial resolution of the sensors.

The resolution of this equation will follow the method described in the paper by Kolodziejczyk et al. 2016 which presents an application for SMOS.

An improvement of this correction has been proposed, particularly regarding the inclusion of SST. This approach remains valid for all L-band sensors.

In principle, correcting the inter-dwell or latitudinal instrument bias does not depend on geophysical conditions. However, suppose the brightness temperature bias (ΔTB) is generally independent of geophysical conditions, especially the sea surface temperature (SST). In that case, this is not the case for the SSS bias (ΔSSS) ([RD09]). Indeed, the sensitivity of the retrieval (transition from brightness temperatures to SSS) depends strongly on SST. The sensitivity of TB

to SSS decreases with a decrease in SST. Therefore, a given ΔTB bias will not have the same impact on SSS at low or high temperatures. More precisely, we have:

$$\Delta SSS = \Delta TB \cdot \left(\frac{1}{\frac{\partial TB}{\partial SSS}(SST)} \right)$$

The lower the sensitivity $\frac{\partial TB}{\partial SSS}(SST)$, the greater the bias on the SSS for a constant TB bias. This behaviour does not simplify the management of bias correction in SSS since, at a given point, SST can vary significantly from one season to another.

If we measure an SSS bias at $SST=SST_0$, it is like measuring a different SSS bias at $SST=SST_1$:

$$\begin{aligned} \Delta SSS(SST = SST_1) &= \Delta SSS(SST = SST_0) \left(\frac{0.015 SST_0 + 0.25}{0.015 SST_1 + 0.25} \right) \\ &\equiv \Delta SSS(SST = SST_0) \cdot \text{coeff}_{SST_0}(SST_1) \end{aligned}$$

$\text{coeff}_{SST_0}(SST_1)$ represents the multiplicative coefficient to calculate the bias when observed at a different SST. So the idea is to compute the bias for a given SST, that is, to reduce each measure to an average SST that does not necessarily correspond to the SST observed at the time of the acquisition.

4.2.2.3 Absolute systematic uncertainties

The $SSS(t)$ estimation from Eqn 4-2 is affected by a global bias, and the $SSS(t)$ estimate essentially contains the SSS anomalies. The relative correction described in the previous section does not allow reaching the absolute SSS field.

The absolute systematic uncertainty calculation requires correction based on climatology or in-situ data. At the SSS level, the resolution of Eqn 4-2 gives L4 SSS anomalies. At this level, it is possible to add these SSS anomalies to a constant shift to reach an absolute SSS.

4.2.2.4 Systematic uncertainties due to TB modelling

Framework

We recall that at Level 2 for a given grid point, the SSS retrieval from satellite Tb measurements (L1c) uses a direct (forward) model, a set of auxiliary data from various variables, the most important ones being SST and wind speed, used either as a first guess (in case of an iterative retrieval process as in SMOS L2OS processor) or as true value to estimate various contributions to be corrected at Tb level before retrieving SSS (as in SMAP and Aquarius RSS processing).

For SMOS, a new L2 reprocessing has been performed:

- using an updated L2OS processor (from the SMOS DPGS L2OS processor v700):

- ❖ Sea state flag bug found and fixed.



- ❖ Sun glint bug found and fixed.
- ❖ BVZ dielectric constant model (instead of BV, see RD17)
- ❖ Best coverage for SSS estimate and Acard estimate.
- ❖ Time coverage -> until end of 2023 (instead of 10/2022).
- ❖ SMOS commissioning period has been reprocessed (01/2010 to 06/2010)

-and using new auxiliary data files:

- ❖ ISAS for OTT computation (instead of WOA)
- ❖ ECMWF ERA5 for auxiliary parameters : WS, SST, Hs, omega ...etc (instead of ECMWF forecast)

For SMAP, the v5.3 has been used instead of v5.0. The new version is corrected from commissioning uncertainties at high latitude north.

4.2.2.4.1 Systematic uncertainties due to RFI

This section presents a method and algorithm developed to mitigate the impact of RFI on SMOS SSS retrievals. RFI sources have intermittently affected SMOS SSS retrievals since the mission's launch in 2010. Our approach focuses on recovering the SSS signal in L2 orbits where intense RFI pollution occurs. The basic method and algorithm are detailed in RD19, in which we provide a prototype example of their application, and the method was applied on three targets in version 4. Recent algorithmic developments have extended the method to the global ocean domain, which is described in this document. The following section outlines the general approach, with more detailed descriptions of the method and global performance results—based solely on SMOS data—provided later.

4.2.2.4.2 General approach

The RFI mitigation method initially employed in three test regions when building CCI L4 products of version 4.4 relied on a regional approach. This approach, referred to as the Regional Method (RM), focused on detecting and correcting RFI contamination over specific regions with known RFI sources. RM worked by analyzing variance across time and space within an area surrounding a recognized RFI source, allowing for the estimation and removal of RFI-induced salinity biases. This method was successfully applied in certain regions, such as around the Samoa Islands, where strong, persistent RFI signals were known to exist.

To extend the RFI mitigation to the entire ocean domain, a hybrid method was developed, integrating both the regional and pointwise methods (PM). The hybrid approach enables global coverage by combining the region-wide capabilities of RM with the pixel-level precision of PM,

overcoming the limitations of regional-only methods, particularly in areas with multiple or intermittent RFI sources.

A key part of our approach involves partitioning the L2 SMOS orbital data into swath intervals across each orbit. Each swath interval contains the true SSS signal but is impacted differently by RFI and other uncertainties. By subtracting the swath-average from the swath-aggregated fields, we effectively characterize the RFI perturbation, enabling the mitigation of its effects. This method ensures that both large-scale and localized RFI patterns are corrected, enhancing the accuracy of SMOS salinity data across the global ocean.

We will provide a detailed description of the method in the following section.

4.2.2.4.3 Method and algorithm

The approach for mitigating RFI contamination in SMOS data has evolved through two key methods: RM and PM, each designed to address specific challenges associated with RFI contamination across different spatial domains.

- **RM:** It focuses on mitigating RFI in a defined region surrounding a known RFI source. The method employs Principal Component Analysis (PCA) to extract a characteristic RFI time series from data within a limited region, typically a circular area with a 100-500 km radius. This time series is then used to characterize RFI contamination over a larger region. RM is particularly effective in areas with consistent, strong RFI sources, as it leverages spatial coherence across the region to correct biases in sea surface salinity (SSS) measurements .
- **PM:** Unlike RM, PM applies PCA at the level of individual pixels, analyzing cross-swath variations in SSS. This approach allows PM to operate without prior knowledge of the RFI source location, making it suitable for areas with multiple or sporadic RFI sources. PM isolates the RFI characteristics at each location, offering a pixel-level correction that can adapt to local contamination patterns . However, it may be less robust than RM in handling large, consistent RFI sources due to its reliance on pixel-level data, which can be sensitive to noise .

Hybrid Method for Global RFI Mitigation (CCI version 5)

To extend the RFI mitigation process globally, a hybrid method was developed, combining the strengths of both RM and PM. This new approach retains RM's regional focus while incorporating the localized precision of PM. The key developments in the hybrid method include:

- 1) **Localized PCA Calculation:** PCA is now computed for each location using data from within a 400 km radius, increasing precision while maintaining regional coherence.
- 2) **Integration of CESBIO Probability Time Series:** This globally available time series allows for an automatic check at each point to determine whether RFI correction is necessary. Corrections are applied only when a strong correlation (above 0.8) is detected between the local PCA component and the CESBIO time series



- 3) Use of Multiple PCA Components: The hybrid method can apply up to two PCA components, enhancing its ability to mitigate strong RFI sources by better capturing the variability in RFI contamination.

This hybrid method is aimed at improving RFI mitigation across the global ocean, providing a more flexible and adaptive solution that is robust against both regional and pointwise contamination patterns. Its purpose is to improve the accuracy of salinity retrievals, particularly in areas with complex or intermittent RFI.

4.3 Uncertainty estimates of SMOS, SMAP and Aquarius SSS.

4.3.1 Introduction

We use L2 and L3 products to characterise the uncertainty on the SSS estimator and get a first idea of the bias behaviour for each sensor.

The quality of the products is assessed by the development team (round-robin tests) and the validation team, which includes the PI-MEP.

We present in this section the estimates obtained in CCI+SSS version 5 products.

4.3.2 External data

In order to compare the SSS of the different sensors with external data, we use the ISAS data and the different comparisons made at PI-MEP. It should be noted that ISAS data are very spatially smoothed (600 km), which can lead to interpretation difficulties when comparing better spatially defined satellite fields over areas where spatial variability is high. In this case, the representativity uncertainties are significant in the comparison mechanism. This representativity uncertainty could be calculated based on high spatial resolution models.

4.3.2.1 PI-MEP (from <https://www.smos-pimep.org/overview.html>)

The Soil Moisture and Ocean Salinity (SMOS) mission was launched on 2nd November 2009 as the second Earth Explorer Opportunity mission within ESA's Living Planet Programme. It has continuously provided brightness temperature data in L-Band since January 2010, which are used to retrieve Soil Moisture (SM) and Sea Surface Salinity (SSS) data over land and ocean, respectively. This project, funded by ESA, aims at setting up a Pilot Mission Exploitation Platform (Pi-MEP), focussing on ESA's SMOS mission and supporting enhanced validation and scientific process studies over the ocean.

Pi-MEP project objectives:

- Focus 1 - Enhanced validation of satellite SSS and products assessment
- Focus 2 - Oceanographic exploitation and case studies monitoring



The **Pi-MEP** is designed to allow **systematic comparisons between available datasets** by providing **comparable QC metrics** for all these SMOS data-derived SSS products and the two other NASA missions. This will enable the following:

1. The user to choose which satellite SSS product is best adapted for their specific application,
2. To improve the Level 2 to Level 4 SSS retrieval algorithms by better systematically identifying the conditions for which a given SMOS, or other satellite, SSS products are of excellent or degraded quality.
3. To converge towards the best approaches and generate less but better satellite SSS products.

A large ensemble of **in situ SSS data distributed by different data centres** can be used to infer SMOS, Aquarius or SMAP SSS data product quality. This includes in situ data from the following sources:

- **ARGO float data** (CORIOLIS)
- **Moored buoy data** (TAO, PIRATA, RAMA, STRATUS, NTAS, SPURS1-2, WHOTS)
- **Thermo-Salinograph** data installed on Voluntary Observing Ships (LEGOS, SAMOS)
- **Thermo-Salinograph** data installed on Research Vessels (GOSUD, Polarstern, NCEI-0170743)
- **Thermo-Salinograph** data installed on Sailing Ships (GOSUD)
- **Surface Drifters** (LOCEAN)
- **Equipped marine mammals** (MEOP)
- **Analysed in situ data fields** (IFREMER/LOPS)
- **Dedicated Campaign data** (e.g. SPURS)

So the PI-MEP is very useful in estimating the quality of the L2OS and L3OS products.

4.3.2.2 ISAS

To cover the entire data record length, we use various ISAS products by order of preference:

-the delayed mode ISAS products created by LOPS laboratory, ISAS17 (reprocessed to avoid drawbacks linked to WOA climatology in the Arctic Ocean, N. Kolodziejczyk, pers. comm.), which includes detailed quality-controlled Argo profiles and other in situ measurements (ships of opportunity, research ships, sailing ships, surface drifters, marine mammals). -For periods when the LOPS product is not available, the delayed mode ISAS product available on Copernicus Marine Environment Service, derived from the objective analysis of different sources of in situ data, mainly Argo floats: http://marine.copernicus.eu/services-portfolio/access-to-products/?option=com_csw&view=details&product_id=INSITU_GLO_TS_OA_REP_OBSERVATIONS_013_002_b

-For periods when none of these products is available, we use the NRT products available on: <http://marine.copernicus.eu/services-portfolio/access-to->



[products/?option=com_csw&view=details&product_id=INSITU_GLO_TS_OA_NRT_OBSERVATIO
NS_013_002_a.](#)

- a new SSS monthly climatology derived by N. Kolodziejczyk (pers. comm) combining an extended SSS database and giving better reference SSS in the Arctic.

4.3.3 Data analysis

4.3.3.1 Introduction

Data analysis is carried out based on the self-consistency of SSS and comparison with ISAS SSS.

A first understanding of the L2 SSS uncertainties comes from each sensor's ATBDs and validation reports.

Random uncertainties must be well known in order to be able to properly weigh the different SSSs when developing L3 and L4 products. We propose to validate the theoretical uncertainties provided in the products or to empirically estimate the uncertainties that affect the SSS estimator (in the case of Aquarius L3 products, such uncertainties are not provided). The theoretical uncertainty (which assumes that the direct model and instrumental response are known) depends on radiometric measurement errors and the sensitivity of TBs to SSS. This sensitivity depends on the sea surface temperature SST. We will therefore characterise the theoretical uncertainty according to SST.

Concerning systematic uncertainties, several causes generate them:

-the instrument, known with a certain level of precision, undergoes poorly controlled and, therefore, poorly corrected solicitations (antenna temperature, antenna gains, etc.).

-the direct model used for inversion is not perfect (dielectric constant, sun, galactic, TEC...)

In all cases, systematic uncertainties result from limited knowledge of the signal and sensor.

The various sensors currently have their own correction strategies at brightness temperature levels.

However, as we will show, there are residual biases (also called systematic uncertainties here) in salinity. Here, we are trying to build a salinity field from salinities from the different sensors. The aim is to mix SSS as homogeneously as possible and thus correct inter-sensor bias.

Two possibilities for addressing these residual biases:

-to improve knowledge of the signal and sensors and to act on brightness temperatures and direct models.

-to compute the bias empirically and to correct it afterwards.



These biases affect the data differently depending on the across-swath position and the orbit type (ascending or descending). More precisely, we know that glint effects depend on the season and the geometry of observation. A solar glint and a galactic glint can, depending on geometry and latitude, have a greater or lesser impact on the signal. Similarly, the flux affecting the antenna back lobes depends on the orientation of the antennas and the position of the different sources and their intensity (for instance, even if the back lobe gains are very low, a source such as the sun can significantly increase the total signal).

We consider that a constant bias affects the following subsets of measurements:

- for SMOS, the same bias is considered for all SSS coming from the same dwell line and position (lat,lon). The dwell lines are sampled across the track every 25 km. The bias has three components: a time-independent component (Land-Sea contamination), a latitudinal seasonal component (coming from sun and galactic contaminations) and a time-dependent component (coming from RFI)

- for SMAP, the bias is considered independently for fore and aft measurements and each (lat,lon) position.

SSS from ascending and descending orbits are also differentiated for both sensors.

- we used the L3 data for Aquarius, ascending and descending orbits separately.

Therefore, we have several datasets from the different sensors, and it is necessary to solve Eqn 4-2 to estimate the biases bc and bl for SMOS. As underlined in section 4.2.2.2, the biases are estimated simultaneously with the SSS optimal interpolation.

4.3.3.2 SMOS L2OS data

During phase 1, particular attention was paid to studying random uncertainties. The theoretical L2 errors multiplied by the chi give a reasonable estimate of the true error far from the coast (section 4.3.3.2.1.1). We have kept the algorithm which increases the theoretical error according to the distance from the coast as developed in phase 1 and presented in section 4.3.3.2.1.2.

In CRDPv5, we sought to improve the corrections to salinities in order to reduce systematic uncertainties (4.3.3.2.2). For this, we worked with two different salinity estimators (SSSuncorr, SSSacard). The salinity estimator provided by the L2OS CCI reprocessing and used in our L4 processing is SSSuncorr. SSSuncorr is obtained after the correction of the TBs by the OTT. We added a bias study from a new SSS estimator, SSSacard, obtained from Acard estimator based on the BVZ dielectric constant model (RD17). Acard is obtained from OTT and LSC corrected TBs but without wind speed inversion during the SSS retrieval. The fact of not estimating the wind speed during the extraction of Acard makes the latter more robust, especially in strong wind speed regions at low SST.

4.3.3.2.1 Random uncertainty

4.3.3.2.1.1 Random uncertainty propagated in the L2OS processor

A maximum-likelihood Bayesian approach is used in the L2 inversion algorithm, taking advantage of *the a priori* information about geophysical parameters (SSS, SST, wind speed, TEC, etc.), hereafter denoted P_i . With this formalism, errors on TB and the retrieved geophysical parameters are assumed to be Gaussian. The following cost function χ^2 is minimised:

$$\chi^2 = \sum_{i=1}^N \frac{[A_{meas\ i} - A_{model\ i}]^2}{\sigma_{Ai}^2} + \sum_{i=1}^M \frac{[P_{j0} - P_j]^2}{\sigma_{Pj0}^2}$$

This means the uncertainty on the a priori P_{j0} (WS, SST ...) parameters is propagated on the SSS estimator.

The theoretical a posteriori variance (uncertainty) $\sigma_{P_i}^2$ can be computed by the Levenberg-Marquardt algorithm as follows (Zine et al., 2008):

$$\begin{bmatrix} \sigma_{P1} \\ \dots \\ \sigma_{PM} \end{bmatrix} = \sqrt{diag(\mathbf{M}^{-1})}$$

Where \mathbf{M} is the pseudo-Hessian, with $\mathbf{M} = \mathbf{F}^T \mathbf{C}_0^{-1} \mathbf{F}$, where \mathbf{C}_0 is the *a priori* covariance matrix and \mathbf{F} the matrix of derivatives:

$$diag(\mathbf{C}_0) = \begin{bmatrix} \sigma_{A1}^2 \\ \dots \\ \sigma_{AN}^2 \\ \sigma_{P10}^2 \\ \dots \\ \sigma_{PM0}^2 \end{bmatrix}$$

The two components of this *a priori* covariance matrix \mathbf{C}_0 are:

- $\sigma_{An}^2 = \sigma_{A_{meas\ n}}^2 + \sigma_{A_{model\ n}}^2$ which includes $\sigma_{A_{meas\ n}}^2$, the estimated instrument brightness temperature uncertainty, and $\sigma_{A_{model\ n}}^2$ the estimated forward model uncertainty. Both are considered in the antenna reference frame. The radiometric uncertainty $\sigma_{A_{meas\ n}}^2$ is already given in the antenna reference frame. The model uncertainty $\sigma_{A_{model\ n}}^2$ is given in the ground reference frame and propagated to the antenna frame before the retrieval (using the ground-to-antenna rotation matrix, see Appendix B of Zine et al., 2008).
- σ_{PMi}^2 , the a priori variance of the geophysical parameter P_{Mi}

Providing the L2OS users with an improved uncertainty σ is critical for several applications, such as proper L2 SSS merging at Level3 and 4 (σ can be used to properly weight multiple L2 SSS observations in a specific space-time window) or for assimilation into Ocean General Circulation Models, etc.

Typically, $\sigma_{A_{meas_n}}^2$ ranges from 1.5 to 3.5 K depending on the distance to the sub-satellite point. Radiometric accuracy is computed based on two main parameters: integration time of the snapshot and footprint size or the equivalent area introduced into the computation of the measurement in the Fourier space. This means that it depends on the incident angle and, therefore, has a cross-track dependency/variation and dwell line dependency. In the first approach, we took the model uncertainty $\sigma_{A_{model_n}}^2$ to be constant and equal to 0.5 K for H and V polarisation and 0.1 K for Stokes-3 and Stokes-4. In addition, in the current version of the processor (v662), the geophysical parameter a priori uncertainties are constant as a function of time and space and given as follows: $\sigma_{SSS} = 100$ psu; $\sigma_{SST} = 1^\circ\text{C}$; $\sigma_{WS} = 2$ m/s and $\sigma_{TEC} = 10$ TECu.

However, the theoretical uncertainty, as described above, is independent on real data; it only relies on the expected characteristics of the measurements and retrieval. To get an uncertainty estimate closer to the real observations, a first improvement has been made by multiplying SSS a posteriori uncertainty by χ , which is the normalised square root of the cost function χ^2 after convergence.

4.3.3.2.1.2 Random uncertainty estimated by using an empirical approach

In order to estimate the actual uncertainties empirically, we consider, for each grid node, time series of 40 days of data taken at different times of the year. The SMOS revisit time is about four days; we have about ten SSS over this period. Assuming that the SSS does not change over this period (which is true most of the time), the std of the time series gives an idea of the uncertainty. However, the uncertainty depends on the position of the measurement according to the centre of the swath. In order to normalise the data, we create a reduced dimensionless centred variable X (normalising by the theoretical uncertainty a posteriori σ_{SSS} multiplied by the χ):

$$X = ((SSS - \langle SSS \rangle) / \widetilde{\sigma}_{SSS}) \quad \text{with} \quad \widetilde{\sigma}_{SSS} = \sigma_{SSS} \times \chi$$

If the theoretical uncertainty is realistic, this new random variable should follow a Gaussian distribution of mean 0 and standard deviation one. If the theoretical uncertainty is underestimated, the std of this new variable is greater than 1. In this way, it is possible to homogenise SSS affected by different theoretical uncertainties.

The histograms of the reduced centred variable are presented in Figure 1, and we note that the distributions are very close to a Gaussian of zero mean and standard deviation 1. The relatively high values of the standard deviation (1.8 and 1.25) are mainly related to distribution tails and the sensitivity of the std to outliers. We can see that the theoretical uncertainty weighted by the χ gives results very close to the error for the open sea. For the coast, there are still high

uncorrected contaminations. They are dominant near the Asian coast, where RFIs are very strong and not temporally stable. In some regions, the high value of the std is due to the dynamics of the SSS over 40 days (rainy areas such as ITCZ and river plumes). In this case, the stability assumption of the SSS is not ensured.

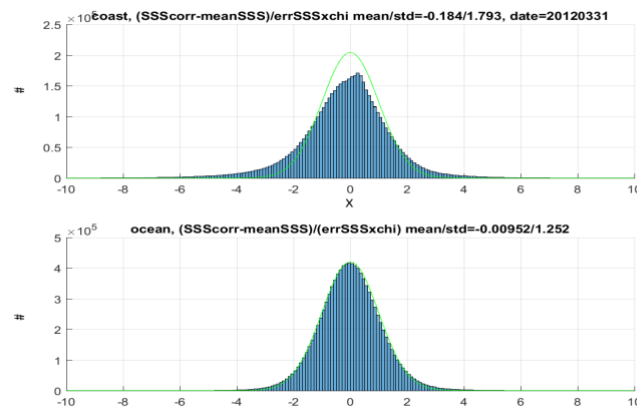


Figure 1: Histogram of the new random variable X (reduced centred SSS) after applying a coastal correction. Top: pixels near the coast ($d_{coast} < 400$ km); bottom: pixels in the open ocean. March 2012.

So, to conclude, the SMOS theoretical uncertainty multiplied by the χ adjustment is, in some cases, underestimated, especially close to the Asian coast and to places heavily contaminated by RFIs. This indicates the presence of outliers. The algorithm of Boutin et al. 2018 allows us to eliminate some of these outliers by adding a 3-sigma filter from data intercomparison.

A specific CCI processing is implemented close to the coast by multiplying the theoretical uncertainty by a factor depending on the distance to the coast $f(\text{dist})$ (see Figure 2).

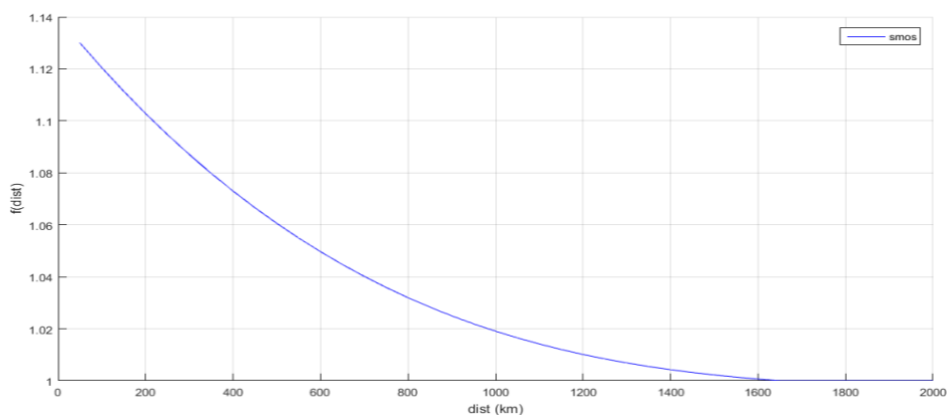


Figure 2: uncertainty factor according to the distance to the coast.

4.3.3.2.2 Systematic uncertainty

4.3.3.2.2.1 Characterisation of systematic uncertainties related to rainfall events

The objective of the CCI is to provide SSS not affected by the instantaneous rainfall. To correct this effect, a first model linking surface freshening and the instantaneous rain rate has been proposed by LOCEAN (Supply, 2020). However, this model does not integrate wind effects. Indeed, vertical mixing is very efficient, especially in strong winds, and the surface effects related to rain are quickly attenuated.

In order to integrate the effect of the wind in the rain correction, we propose to start from the LOCEAN model, with an additional weight by the wind, following an adaptation of the model proposed by (RD15):

$$dSSS = a_0(RR) \cdot WS^{-1.1}$$

With $a_0(RR)$, the freshening corresponds to an instantaneous rain rate (RR) for a wind speed (WS) of 1m/s. The original model predicts freshenings an order of magnitude lower than the ones observed on SMOS SSS as a function of IMERG RR. In order to calibrate the Drushka formalism with satellite observations, we will take as $a_0(RR)$ the correction obtained by A. Supply from freshening data taken on the ITCZ region after integrating it on all wind speeds.

The relation proposed by Drushka et al. (RD15) does not fit well with satellite observations, likely due to inhomogeneous conditions in satellite pixels integrated in ~ 50 km. Moreover, the correction can reach very large (infinite) non-physical values for very low wind speeds. Therefore, it is necessary to choose a wind speed cutoff below which the correction no longer depends on the wind speed. The new relation which integrates this WS_{min} cutoff is written as follows:

$$dSSS(RR, WS \geq WS_{min}) = a_0(RR) \cdot WS^{-1.1} / \langle WS^{-1.1} \rangle$$

$$dSSS(RR, WS < WS_{min}) = a_0(RR) \cdot WS_{min}^{-1.1} / \langle WS^{-1.1} \rangle$$

$\langle WS^{-1.1} \rangle$ is the weighted average of WS over the ITCZ region, equaling 0.17. Note that this average is only slightly dependent on RR. With this formulation, we ensure the continuity of the correction according to the wind and avoid over-corrections at very low winds. Moreover, it allows us to recover the $a_0(RR)$ correction of A. Supply was obtained by averaging the freshening in the ITCZ region overall wind speeds (see A. Supply, 2020 PhD thesis, <https://theses.hal.science/tel-04024079>)).

To choose the WS_{min} cutoff, we selected heavy rainfall events. We compared the corrected SMOS SSS with the ISAS SSS (over areas of low variability) under different wind cutoffs and over the period [2015, 2016]. Figure 3 shows the histograms of the SMOS-ISAS residuals after the rain correction for regions of high SST.

Figure 4 shows the median(SMOS-ISAS) and std(SMOS-ISAS) as a function of the WSmin cutoff. The WSmin cutoff is chosen such as the one which minimises the std and the absolute value of the median differences.

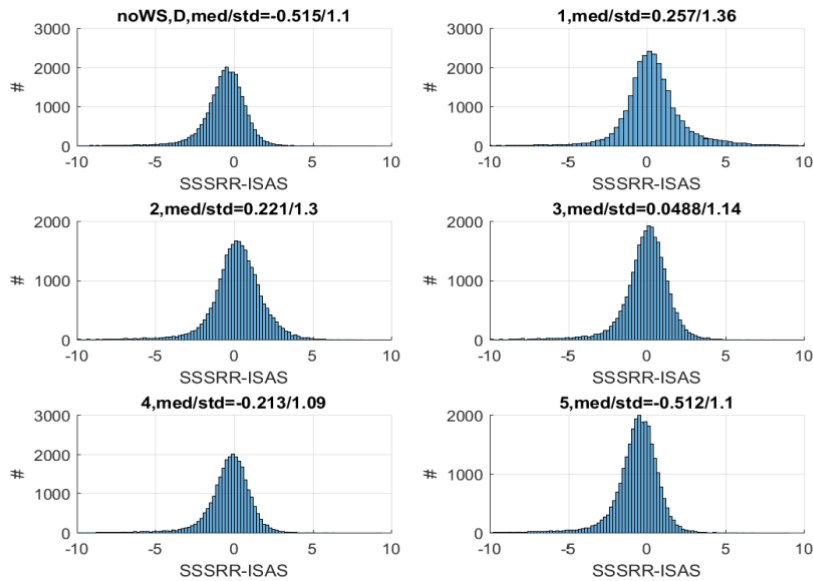


Figure 3: Corrected SSS – ISAS SSS with different WSmin cutoffs in case of heavy rain and high SST (>25°C). Top left, WS-independent a0(RR) correction; then, from top to bottom and from left to right, WSmin cutoff taken at 1, 2, 3, 4, 5m/s respectively. Median and std differences are reported in the title of the figures for each WSmin cutoff.

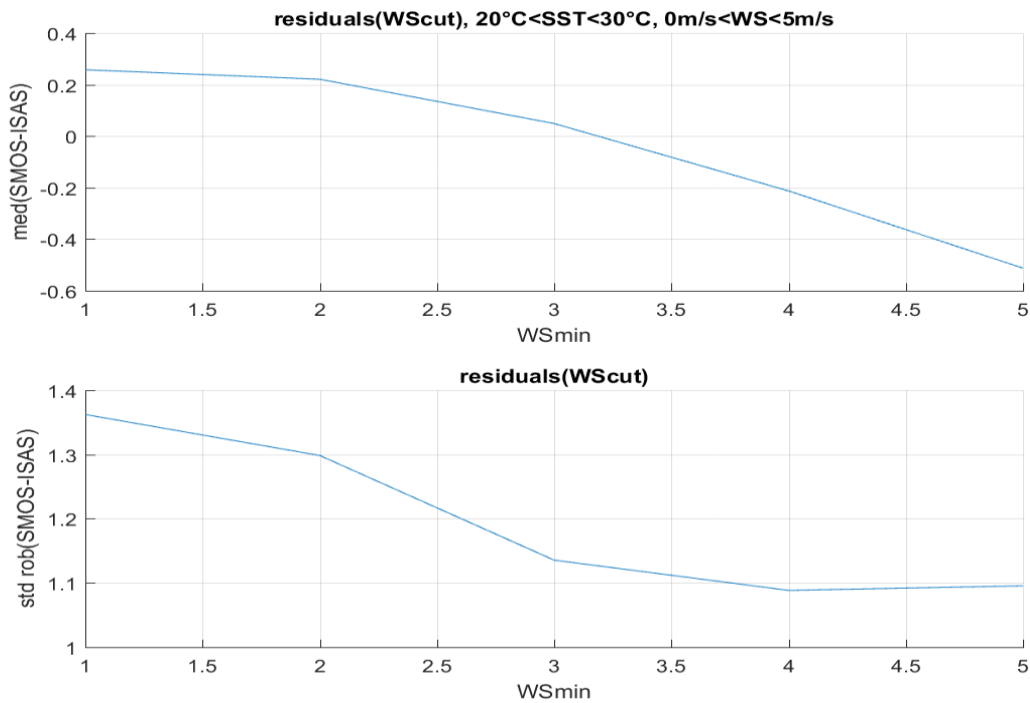


Figure 4. Top: median(SMOS-ISAS) as a function of the WScut parameter chosen as cut-off. Bottom: std(SMOS-ISAS).

We did the same for regions with a low SST (Figure 5 et Figure 6).

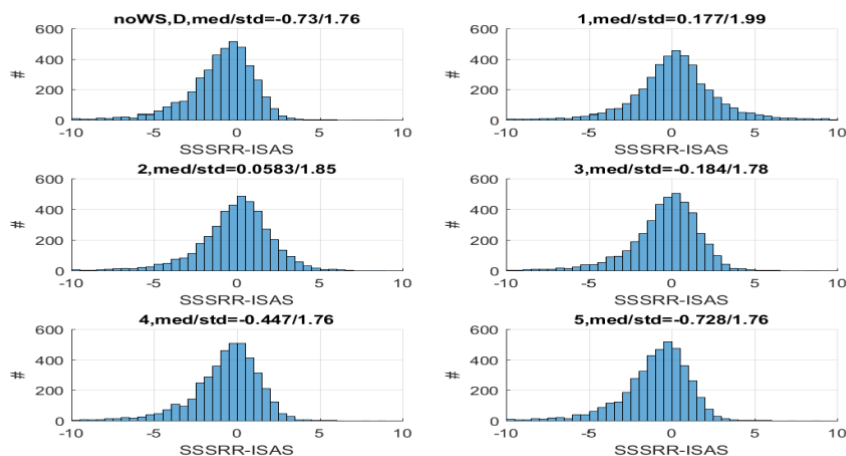


Figure 5: idem Figure 3 with an SST between 10 and 20°C

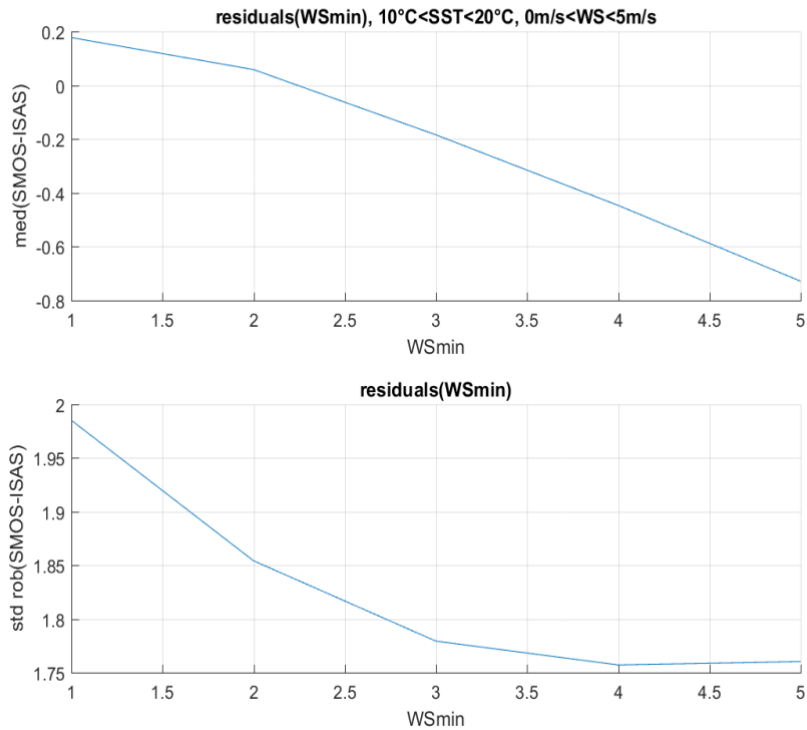


Figure 6: idem Figure 4 with an SST between 10 and 20°C

In the two SST cases presented, the minimum of std(SMOS corrected - ISAS) is around 4m/s. The bias, on the other hand, has a minimum around 2 or 3 m/s.

Based on these results, we took a cutoff value of WSmin=3.5m/s.

The freshening correction according to the RR for various wind speeds is presented in Figure 7:

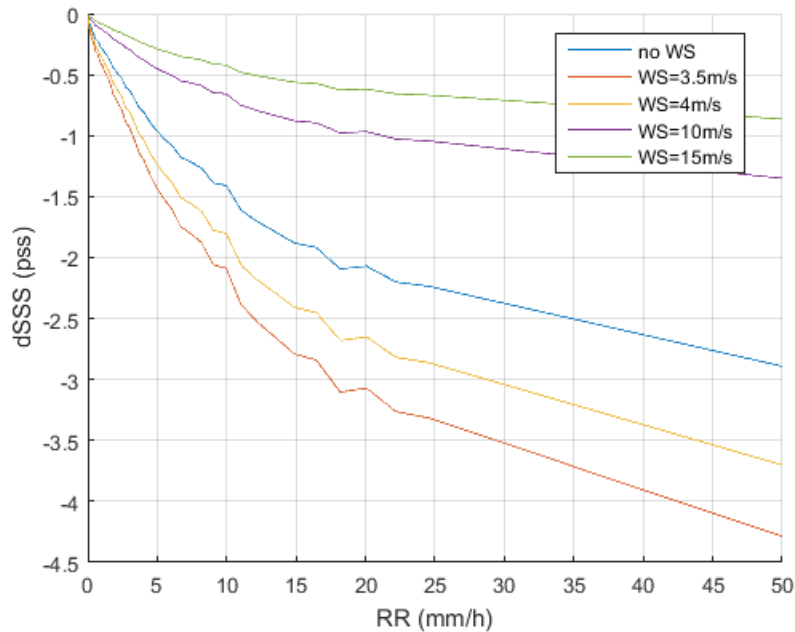


Figure 7: correction of the effect of rain on SSS according to various WS. The correction integrated overall wind speeds is shown as a blue curve.

In Figure 7, the blue curve shows the $a_0(RR)$ correction, which is applied on CCI+SSS version 3 based on the work of Alexandre Supply (RD16). The other curves correspond to the CCI+SSS V4 correction for winds ranging from 3.5 to 15m/s. The curve at 3.5m/s corresponds to the maximum possible correction given the choice of $WS_{min}=3.5m/s$.

4.3.3.2.2 Characterisation of systematic uncertainties related to the dielectric constant

In CCI+SSS V4, the L2 SMOS SSS are retrieved with the BV dielectric constant model (Boutin et al., 2020) implemented in the L2OS processor version 7. This model has been updated recently with an adjustment of the Debye model based on laboratory measurements instead of SMOS measurements. The new parametrisation is called BVZ (RD17). This new setting has been used in CCI+SSS V5.

4.3.3.2.3 Characterisation of systematic uncertainties related to wind speed

In order to characterize systematic uncertainties related to wind speed, the starting point is the SSS corrected for rain and dielectric constant effects.

To characterize the systematic effects related to the wind model, we select observation conditions not strongly affected by other uncertainty sources by considering the following criteria:

- SSS variability < 0.1
- Descending orbits (in order to avoid strong ice contamination in the Southern Ocean)
- $abs(xswath) < 200km$

- $Fg_sunglint = 0$
- Data outside the eastern equatorial Pacific region [$abs(lat) < 5^\circ$ for $-180^\circ < lon < -80^\circ$] known to experience large positive biases, likely related to strong currents.

According to the investigations performed by N. Reul in the frame of the ESA L2OS studies, the correction is expected to depend on the sea states. Here, two classes of sea states are considered: a class dominated by the wind sea, called "wind" hereafter, and a class dominated by swell, called "swell". These two classes are identified by sea state flags in the L2OS V7 product (see table below). A bug concerning the classification has been detected in the L2OS V7 processor and has been fixed (this bug affects CCIv4 products). Moreover, the use of ERA5 data for classification allows avoiding the effect of the ECMWF processing changes and allows obtaining homogeneous time series of the flags over the whole period.

The occurrence of the sea states is given as a function of time in Figure 8. We merged the six classes into two classes (swell and wind classes).

Table 1: L2OS sea states

| | |
|------------------------------|---|
| $Fg_sc_sea_state_1[Ngp]$ | Sea state class 1: waves wind dominated, old sea. Flag set if swell fraction $< Tg_swell$ and $\omega < Tg_old_sea$ |
| $Fg_sc_sea_state_2[Ngp]$ | Sea state class 2: waves swell dominated, old sea. Flag set if swell fraction $\geq Tg_swell$ and $\omega < Tg_old_sea$ |
| $Fg_sc_sea_state_3[Ngp]$ | Sea state class 3: waves wind dominated, medium sea. Flag set if swell fraction $< Tg_swell$ and $\omega \geq Tg_old_sea$ and $\omega \leq Tg_young_sea$ |
| $Fg_sc_sea_state_4[Ngp]$ | Sea state class 4: waves swell dominated, medium sea. Flag set if swell fraction $\geq Tg_swell$ and $\omega \geq Tg_old_sea$ and $\omega \leq Tg_young_sea$ |
| $Fg_sc_sea_state_5[Ngp]$ | Sea state class 5: waves wind dominated, young sea. Flag set if swell fraction $< Tg_swell$ and $\omega > Tg_young_sea$ |
| $Fg_sc_sea_state_6[Ngp]$ | Sea state class 6: Waves swell dominated, young sea. Flag set if swell fraction $\geq Tg_swell$ and $\omega > Tg_young_sea$ |



Figure 8: Number of flags raised as a function of time for the 6 L2OS classes from ERA5 model

The bias on the SSS is characterised in the (WS, SST) plane: $b_{SSS}^{obs}(WS, SST)$. If the bias of the modelled TB is independent of the SST, then the effect on the estimated SSS depends on the SST due to the dependence of $\partial Tb / \partial SSS$ with SST. It is estimated with the following relationship:

$$b_{SSS}^{theo}(WS, SST) = b_{SSS}(WS, 15^\circ C) \cdot (0.015 \cdot 15 + 0.25) / (0.015 \cdot SST + 0.25) \quad \text{Eqn 4-3}$$

where $b_{SSS}(WS, 15^\circ C)$ is the estimated wind speed related bias at $SST = 15^\circ C$. According to this equation, for a given bias in TB, the SSS bias should not change of sign if the model bias in TB is independent of SST. Figure 9 shows that this is not the case for $WS < 4m/s$ in case of a swell, suggesting that for low wind speeds, the Tb bias is not independent of SST. For this reason, the correction at $WS < 4m/s$ is done without following Eqn 4-3.

The SSS biases in the (WS and SST) plans were calculated for SSScorr and SSSacard. The SSSacard behaves differently, which can be explained by the fact that the wind components are not retrieved during the retrieval, while this retrieval may be affected by an error in the wind model and/or in the dielectric constant model. The correction applied to Acard will therefore be specific. The $b_{SSS}(WS, 15^\circ C)$ correction is obtained from the bias given in the (WS, SST) plane based on a least squares algorithm. It is estimated separately for the wind and swell class (Figure 10).

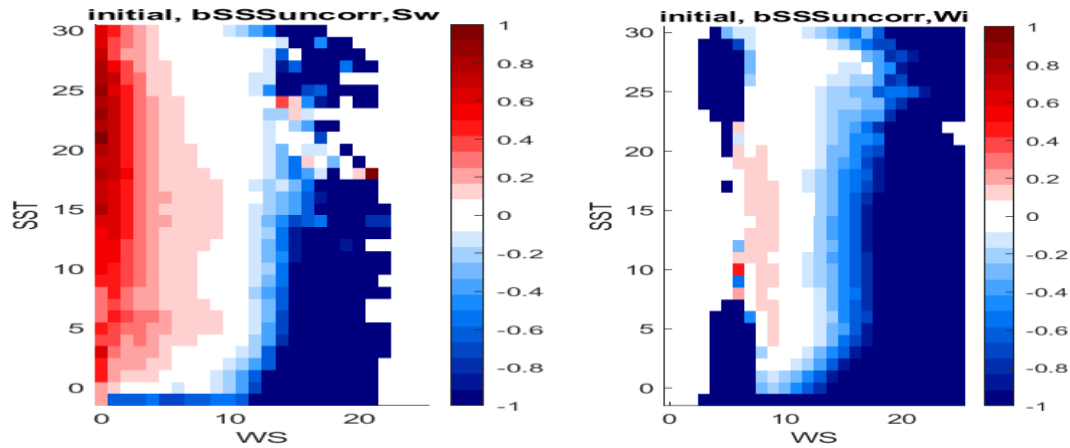


Figure 9: SSS biases in the (WS,SST) plane (descending orbits). Left: roughness dominated by the swell; right: roughness dominated by the wind sea.

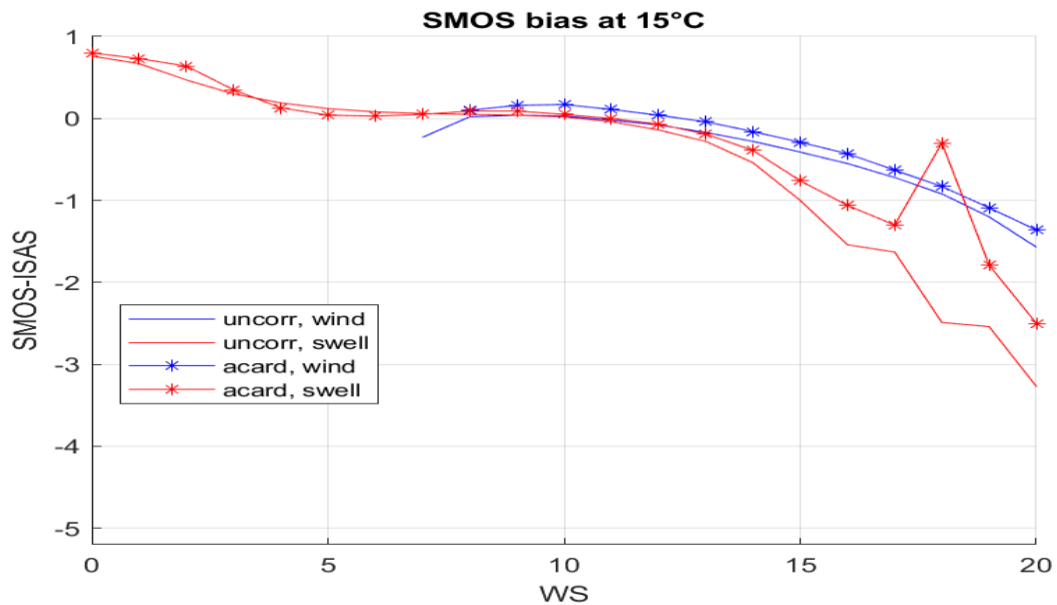


Figure 10: Correction at 15°C for the 3 SSS (uncorr, corr and acard) and the two sea classes (swell and wind).

Given these results, the correction algorithm for a satellite pass over a given grid node (to which we associate two estimators of the SSS: SSSuncorr and SSSacard) follows the following steps:

-identification of the class to which the SSS belongs according to the sea state flags (wind or swell)

-if the SSS belongs to the wind class, the correction calculated at 15°C is applied to the effective SST (bSSStheo) for the SSSuncorr and SSSacard cases.

-if the SSS belongs to the swell class with a $WS > 4\text{m/s}$, the correction calculated at 15°C is applied to the effective SST (bSSStheo) for the SSSuncorr and SSSacard cases.

-If the SSS belongs to the swell class with a $WS < 4\text{m/s}$, the bSSS_obs correction is applied.

4.3.3.2.2.4 Characterisation of latitudinal seasonal systematic uncertainties

A bias depending on latitude and season was quantified (Boutin et al. 2018). Therefore, we are in the situation of Eqn 4-2 with 2 biases to manage (latitudinal and inter-dwell biases).

SMOS data is affected by latitudinal and coastal systematic uncertainties (biases).

The latitudinal bias was estimated under the following conditions:

- Period [2013-2023].
- Pseudo-dielectric constant (Acard) filtering ($|\text{Acard smos} - \text{Acard mod}| < 4$). This filtering allows removing part of the ice and RFI contaminations.
- Filtering of SSS with large random uncertainty (L2 SSS random uncertainty < 20)
- Filtering of SSS which pertains to the outside reasonable interval ($\text{SSS} > 42$ or $\text{SSS} < 5$)
- Filtering of SSS with $WS > 16\text{ m/s}$
- Distance to the coast $> 600\text{km}$. Exclusion of some regions strongly affected by RFIs. The selected area for latitudinal computation is given in Figure 11.
- Smoothing of the correction with a 5° latitude window width (instead of 10° in version 1)
- Reference SSS from ISAS: ISAS 17 + delayed and NRT products
- Selection of ISAS SSS explaining a significant amount of variance (with PCTVAR $< 80\%$)

In order to characterise the latitudinal seasonal systematic uncertainties, SSS corrected for rain, dielectric constant and wind effects are used.

It is assumed that the LSC does not contaminate the open ocean data. Data are selected at 600km from the coast (if a too large limit is taken, it is impossible to calculate the correction

north of 45°N). A mask is added over the North Pacific and the Indian Ocean, which RFI contamination affects.

The latitudinal biases depend on the season (solar and galactic contamination, eclipse period), the type of orbit (ascending or descending) and the acquisition geometry. The latter is characterised by the distance of the acquisition from the satellite track expressed in km and called swath in the following.

In order to estimate this bias, we use ISAS as a reference. The ISAS data are filtered on a PCTVAR criterion (< 80) and a variability criterion ($< 0.1\text{ps}$). In order to cover all latitudes, in case of coverage problems, the filtering criteria of the ISAS data are relaxed.

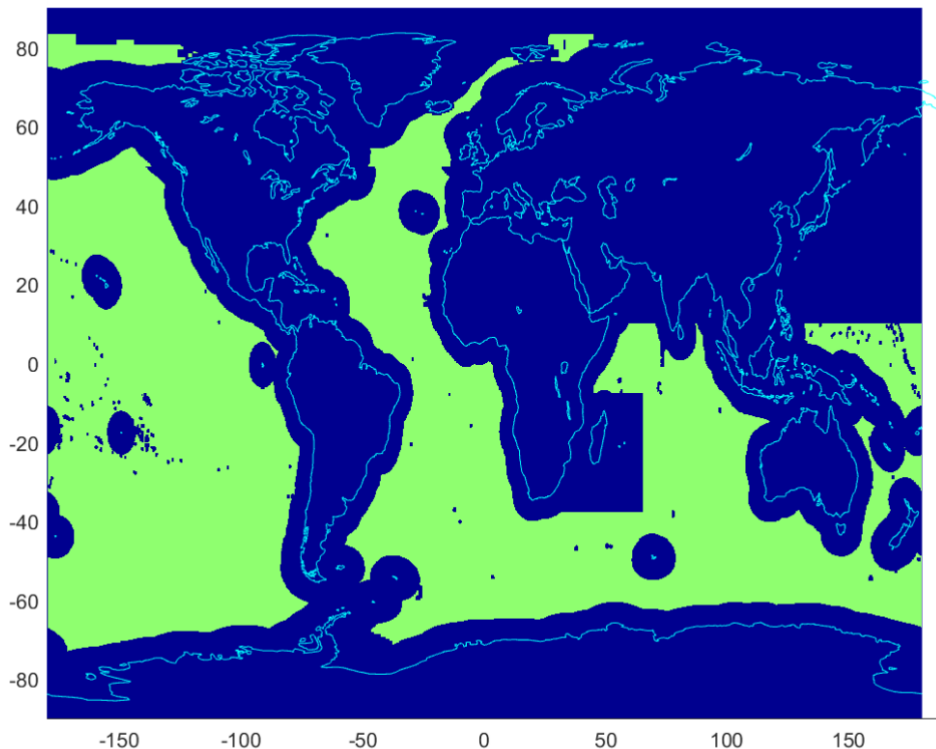


Figure 11: Mask for seasonal latitudinal correction

We keep the CATDS latitudinal correction already applied for the beginning of the period.

The following figures (Figure 12) show, for some cases, the estimated latitudinal biases for SSSuncorr and SSSacard, the month of June.

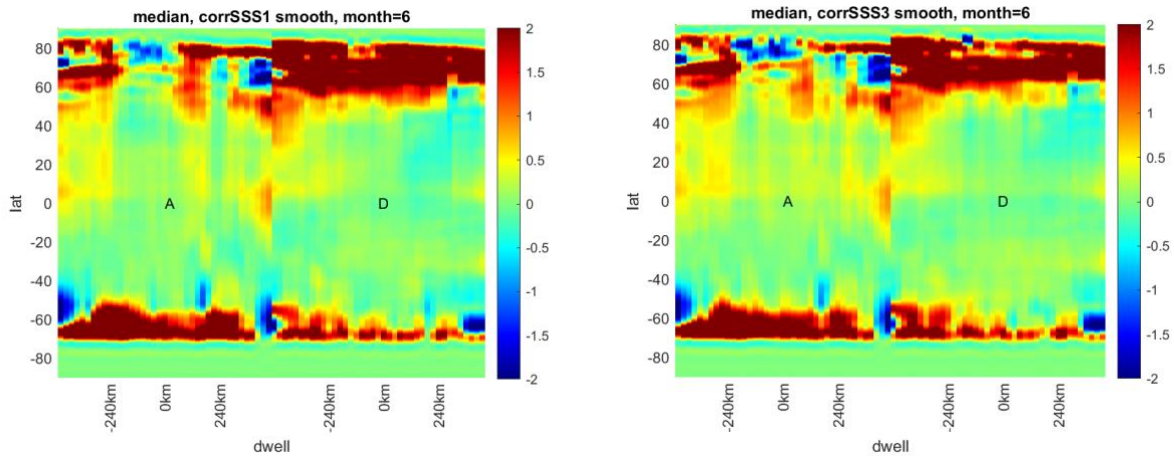


Figure 12: example of latitudinal correction for the 2 SMOS SSS (SSSuncorr on the left and SSSacard on the right). Ascending dwells are shown on the left-hand side of each figure, descending dwells on the right-hand side. Month of June. The y-axis gives the distance from the track in km.

Once the correction has been applied, a check on the effect of the correction is required, in particular, to identify inter-annual biases that could not be corrected because of the seasonal assumption. The largest part of the biases is well corrected except in certain situation where the bias has some inter-annual signature, especially during descending orbits in 2014 and 2015, north hemisphere (Figure 14). Ascending orbit correction behaves more homogeneously (Figure 13). Some inter-annual signatures appear at high latitudes.

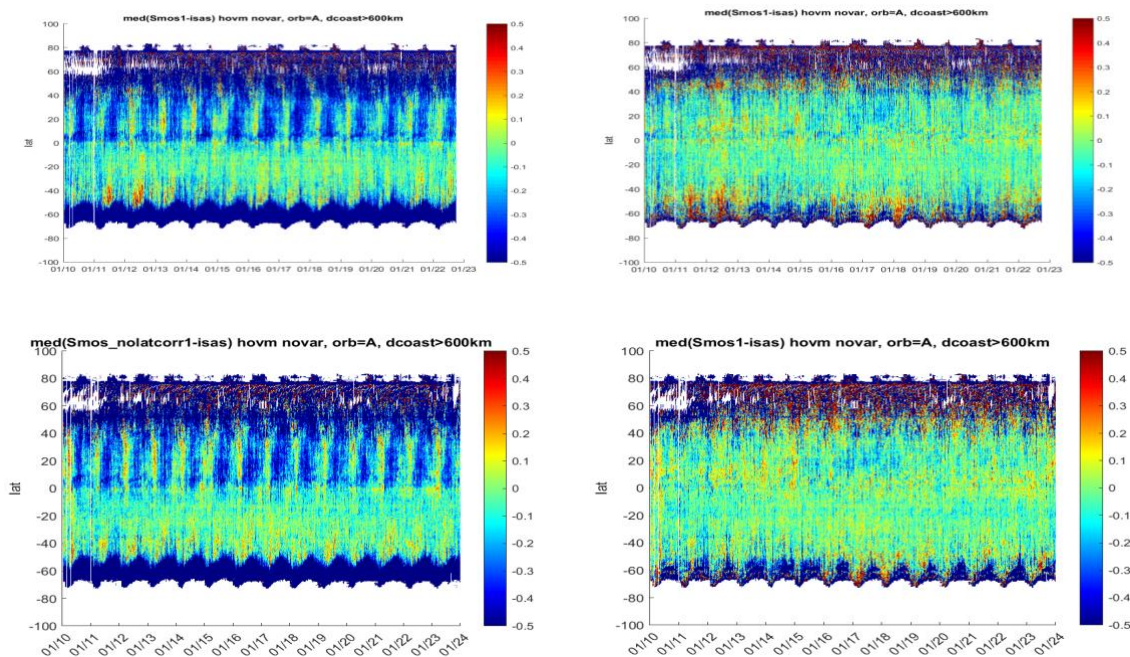


Figure 13: Hovmoller of the difference between SSSuncorr and ISAS, ascending orbits. Left: before latitudinal correction; right: after latitudinal correction. Top, CCIv4; bottom, CCIv5.

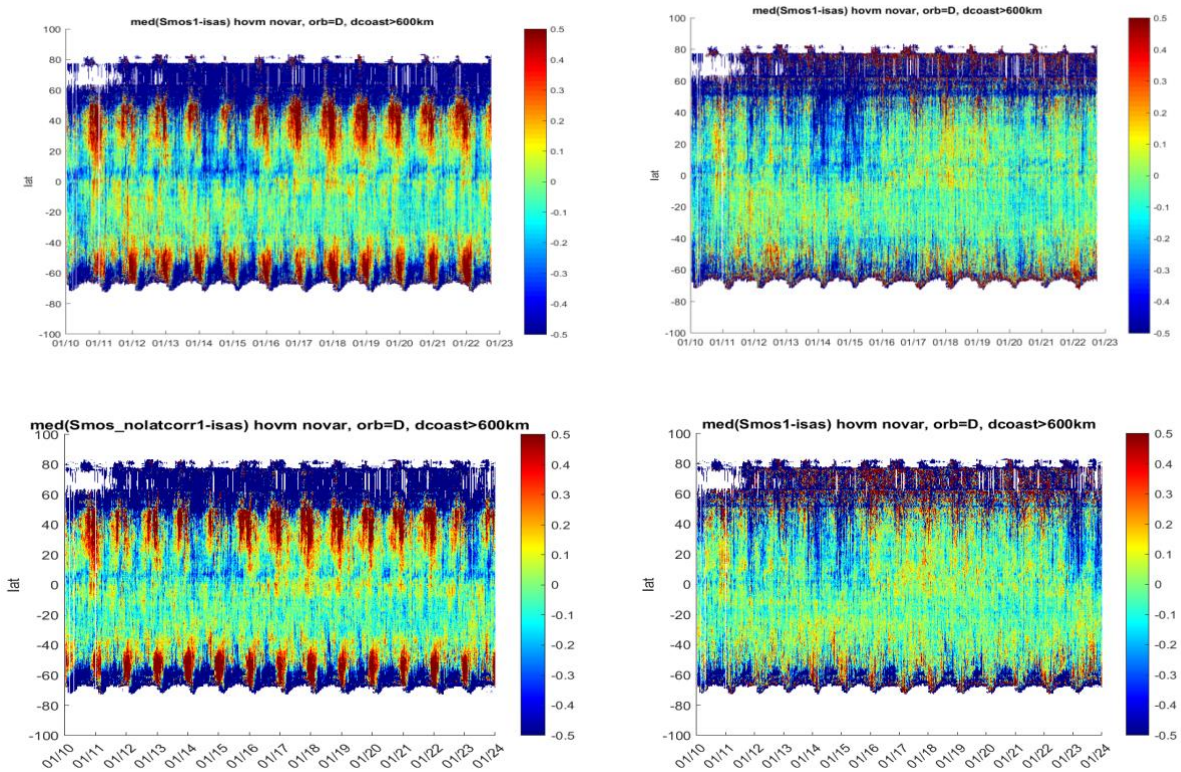


Figure 14: idem than Figure 13 for descending orbits.

4.3.3.2.2.5 Characterisation of RFI systematic uncertainties: A Prototype Example of the RM Method.

We present results for the Samoa region (178.255°E, 198.255°E, 23.874°S, 3.874°S) in the southwestern tropical Pacific, highlighting the capabilities of RM as a prototype example of its application to correct RFI contamination. See RD19 for an exhaustive description.

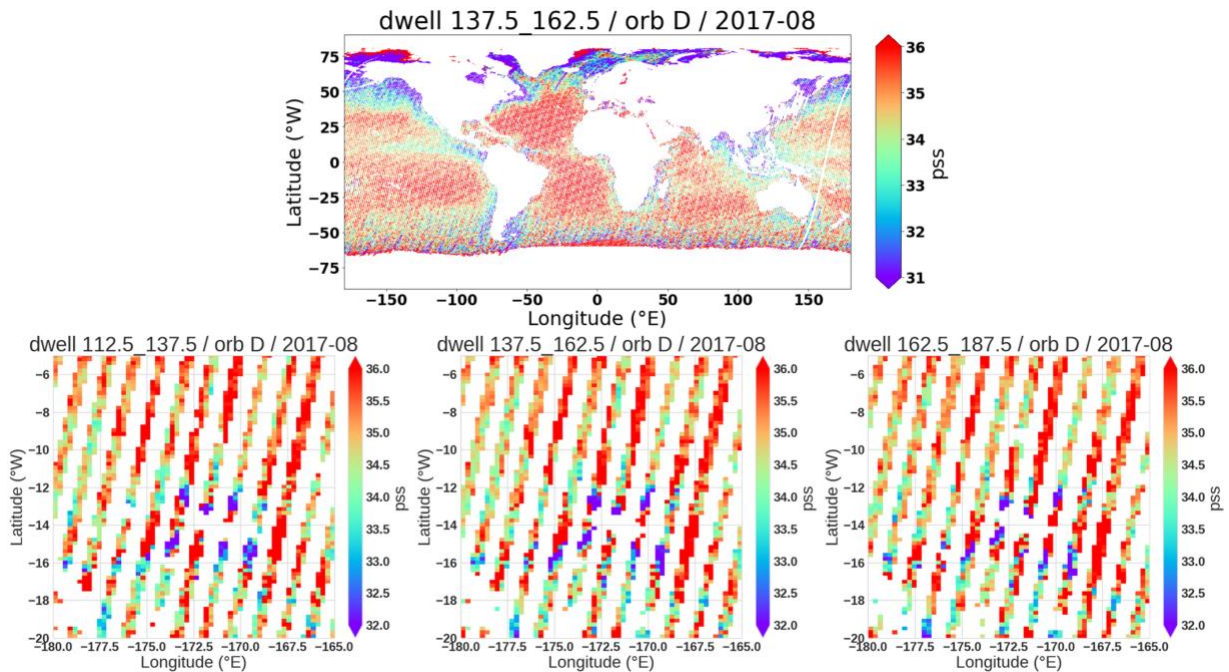


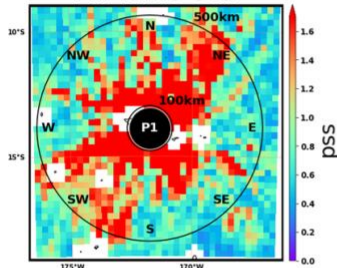
Figure 15: (Top) Monthly global map including swath interval $[+137.5\text{km},+162.5\text{km}]$ of SSS for all descending half orbits in August 2017. (Bottom) Zoom in over the Samoa region for $[+112.5\text{km},+137.5\text{km}]$, $[+137.5\text{km},+162.5\text{km}]$, $[+162.5\text{km},+187.5\text{km}]$ intervals of descending half orbits for the same month.

The RFI correction process consists of several key steps, outlined below. The maps and figures illustrate the RM method's ability to effectively characterize and mitigate RFI contamination, leading to significant improvements in SSS retrievals. Figure 15 presents monthly agglomeration maps for August 2017, showing low salinity levels in the Samoa region indicative of RFI pollution. Figure 21 further illustrates the swath-interval differences with a star-like structure characteristic of RFI disturbance, and Hovmöller plots that emphasize the onset and impact of the RFI source. The Principal Component Analysis (PCA), applied to swath-interval differences, highlights that the first PCA mode explains about 60% of the variance. The time series shown in Figure 17 characterizes the timing of the RFI contamination. The spatial structures associated with the correction are presented in Figure 18, where we zoom in on a small area around the RFI source to showcase the features of the correction.

A[-287.5/-262.5]km-D[-262.5/-237.5]km

Abs Diff SSS

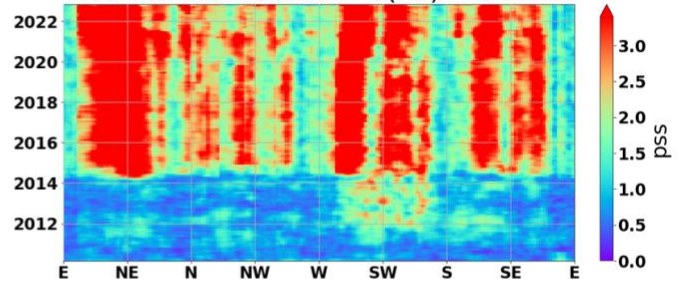
All-Time Std



A[-287.5/-262.5]km-D[-262.5/-237.5]km

Abs Diff SSS

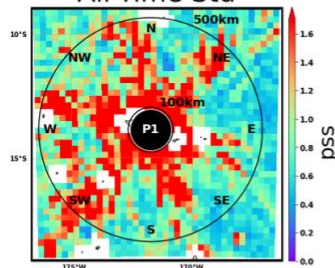
Mean within 100km < d(P1) < 500km



A[-212.5/-187.5]km-A[+387.5/+412.5]km

Abs Diff SSS

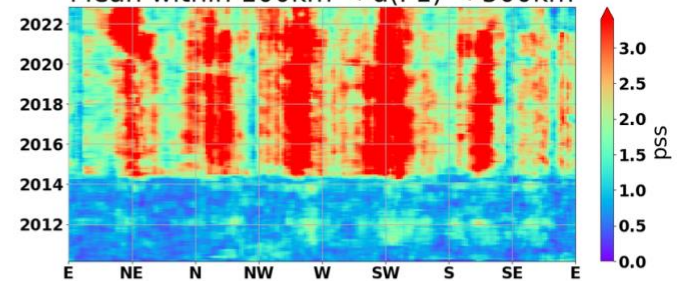
All-Time Std



A[-212.5/-187.5]km-A[+387.5/+412.5]km

Abs Diff SSS

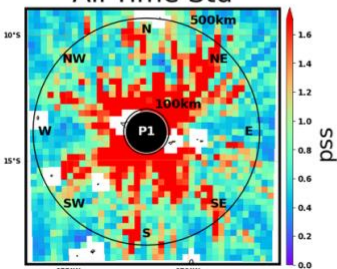
Mean within 100km < d(P1) < 500km



A[-187.5/-162.5]km-D[+37.5/+62.5]km

Abs Diff SSS

All-Time Std



A[-187.5/-162.5]km-D[+37.5/+62.5]km

Abs Diff SSS

Mean within 100km < d(P1) < 500km

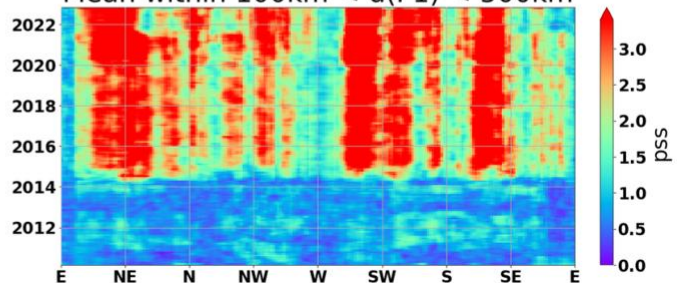


Figure 16: Examples of swath-interval differences calculated from the 11-month moving averaged SSS swath intervals. (Left) Maps of the std over the entire period of the absolute difference of various 11-month m.a. swath-interval fields. (Right) Angular hovmöller plots where directions E, NE, ... are indicated in the rose around the source (P1) on the Left and where SSS is averaged over the angular sectors diverging from the source.

The unique corrective time series, illustrated in Figure 19, is used to build the space-time correction for the region. Figure 20 demonstrates the correction process for a specific swath interval, showing the initial and corrected dwell field anomalies, with the right panel displaying

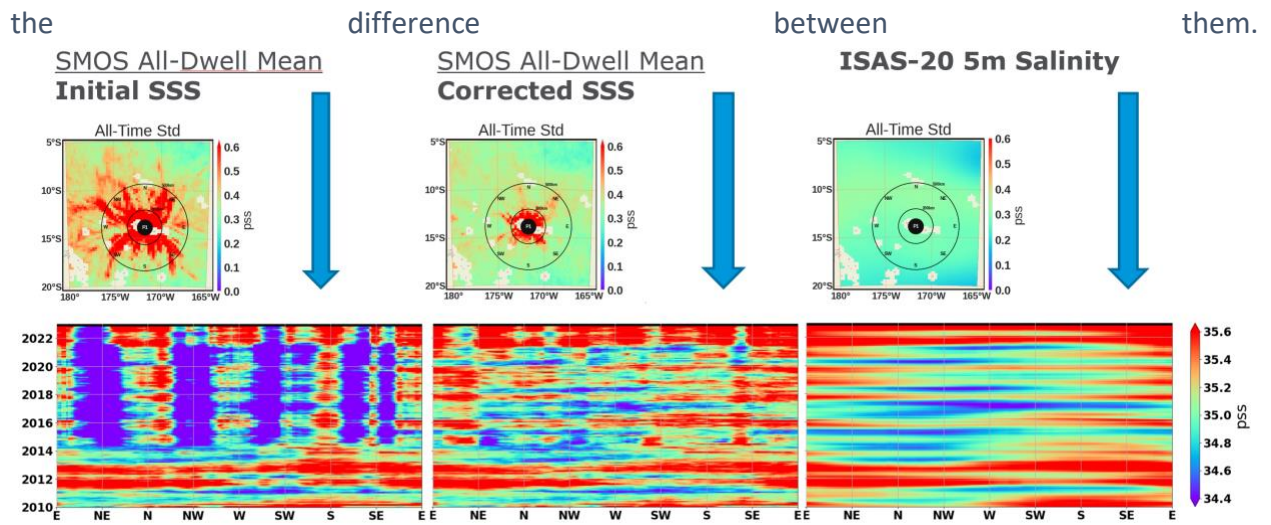


Figure 21 demonstrates the improved performance of the correction method over time. The corrected space/time field is closer to ISAS20, and SSS variability is significantly recovered from below the initial RFI pollution. Finally, Figure 22 depicts the evolution of a comparison metric with respect to ISAS20, revealing that the RFI perturbation has been effectively filtered out, resulting in corrected SSS that more closely matches ISAS20.

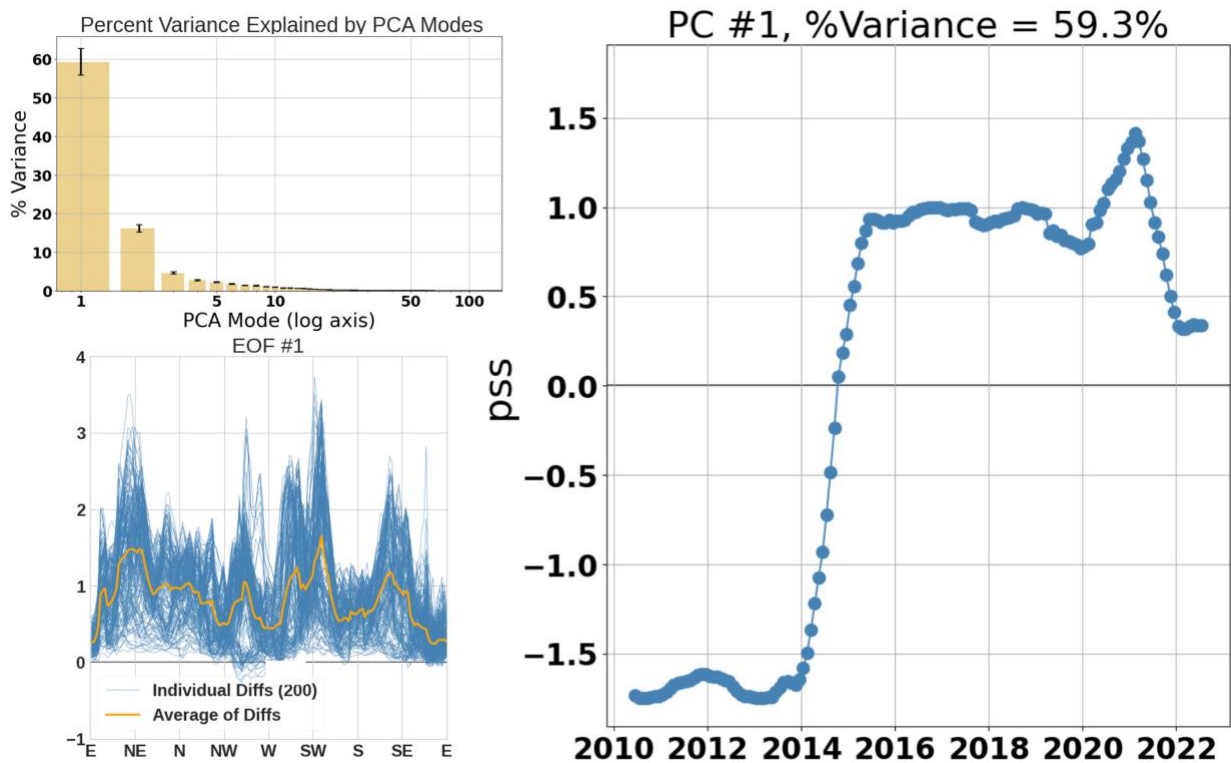


Figure 17: 1st mode results of the PCA applied to the dwell-line differences. (Top-Left) Percentage of variance explained by the PCA modes as a function of the mode number. (Top-Right) The time series is associated with the first mode (in pss). (Bottom-Left) Spatial structures of the first mode are given in angular sectors around the RFI source.

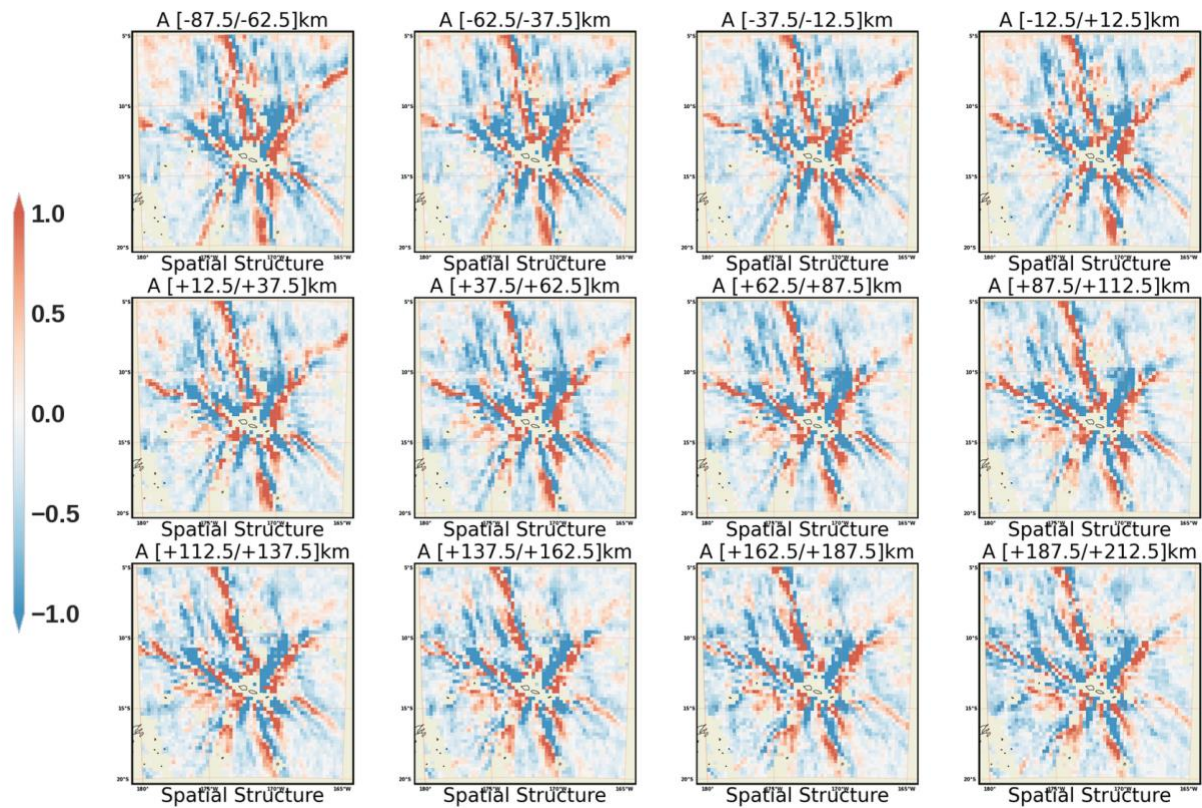


Figure 18: Portion of the spatial patterns related to the initial regression utilized to compute $V'_0(d_k, x, y)$, which is the spatial element of the correction package.

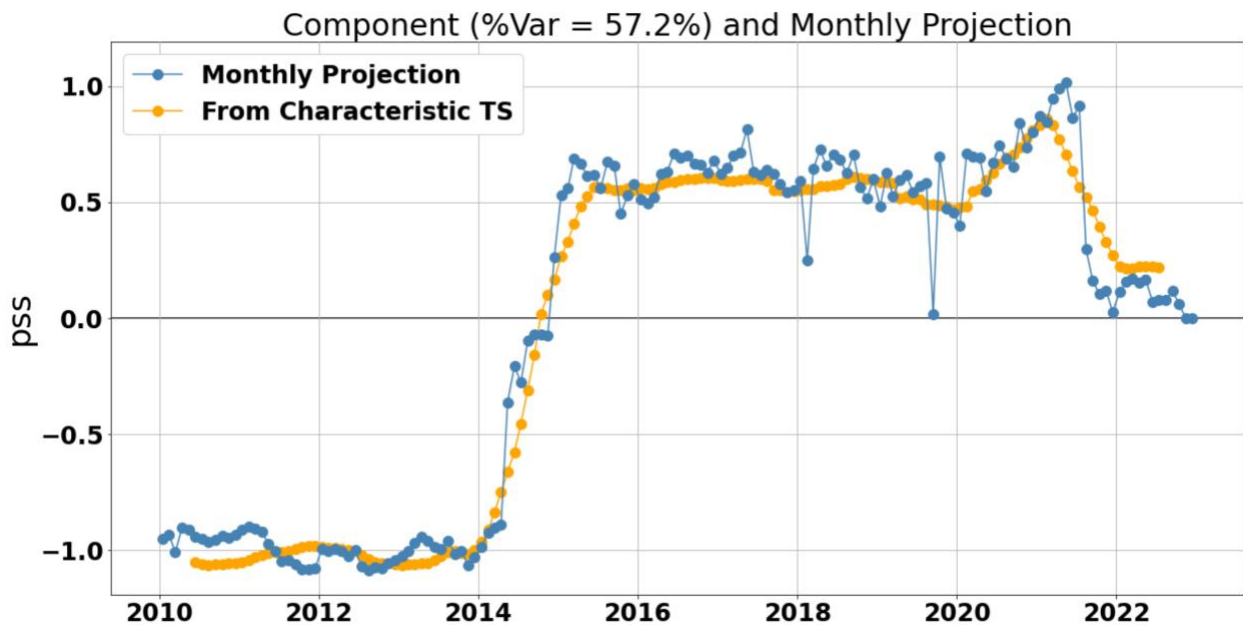


Figure 19: (Blue) Monthly RFI characteristic time series $U_0^1(t)$ obtained by projecting the monthly dwell-line agglomerates onto the RFI spatial structures. (Orange) The (11-month m.a.) characteristic time series previously calculated is superimposed for comparison.

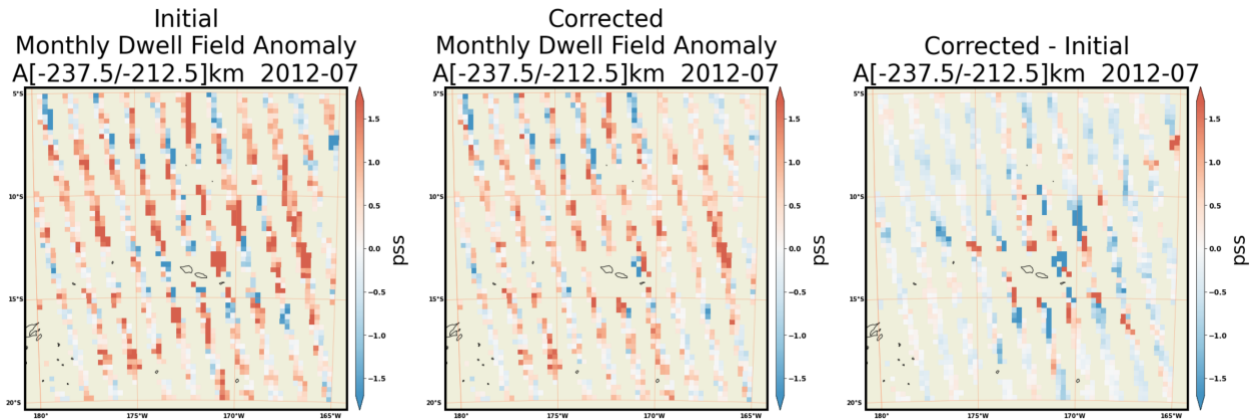


Figure 20: Example of correction for a specific dwell line (Ascending, -237.5km,-212.5km) in July 2012. (Left) Initial dwell field SSS anomaly (with respect to time mean). (Middle) Corrected dwell field anomaly. (Right) Difference between corrected and initial fields.

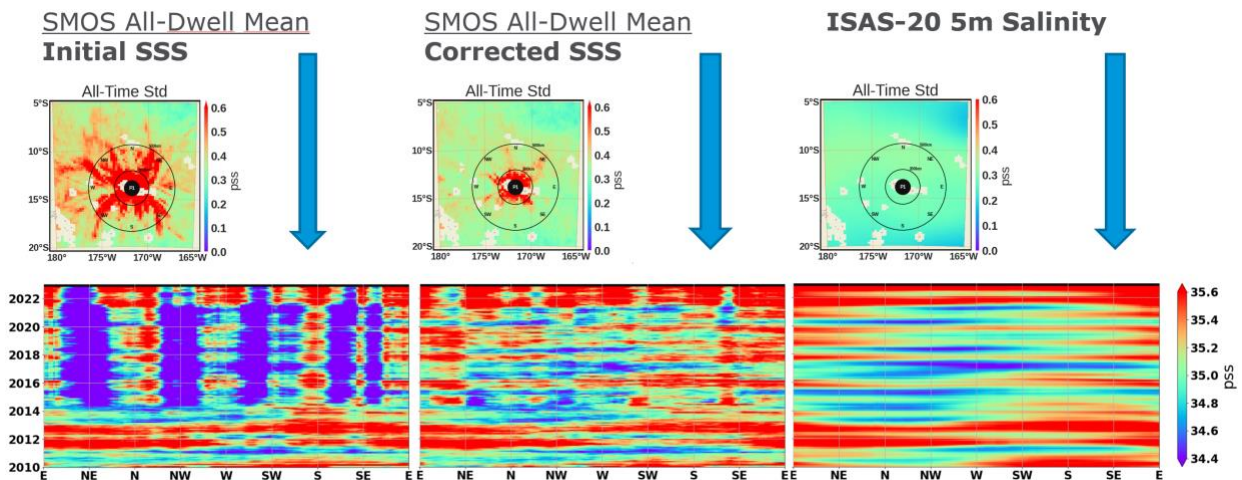


Figure 21: Performance of the correction method with respect to ISAS-20 5m salinity. Here we average SSS over all the dwell lines, add a constant time-mean field, and look at angular hovmoller variations around the source (Left) All-dwell mean of initial SSS. (Middle) All-dwell mean of corrected SSS. (Right) ISAS20 5m salinity.

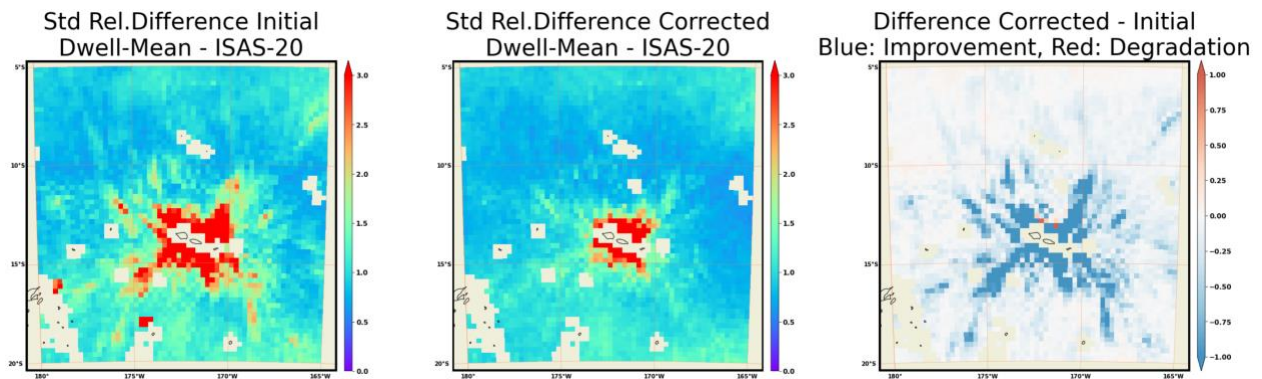


Figure 22: Performance of the correction method with respect to ISAS-20 5m salinity. Here we calculate and plot a performance metric with respect to ISAS20 at each grid point. All dwell SSS are preliminarily averaged. (Left) Plot of the metric $\frac{std(sat - isas)}{std(isas)}$, for the initial SSS dwell data. (Middle) Plot of the same metric for the corrected SSS dwell data. (Right) Difference (Middle)-(Left), that highlights improvement (blue) or degradation (red) with respect to ISAS20.

4.3.3.2.2.6 Results of the Hybrid Method

The hybrid RFI mitigation method, which integrates the strengths of RM and PM, is now applied across the entire ocean domain. To demonstrate its effectiveness, we focus on three historically treated regions—Samoa, Barbados, and the Guinea Gulf—previously addressed in RD19 and CCI version 4.4. These regions illustrate the method's performance in mitigating RFI contamination.

The Figure 18 shows the performance of the hybrid method relative to ISAS20, with the std metric highlighting improvements (blue) and degradations (red). Around Samoa, the method not only treats the local RFI contamination but also extends its correction to nearby areas, such as the Fiji Islands. Similarly, in the Barbados region, RFI pollution is mitigated both around Barbados and the Dominican Republic. In the Guinea Gulf region, while the improvements are less pronounced, the method reduces the impact of RFI in areas with moderate contamination.

These results, based solely on SMOS data, reflect the expected performance of the hybrid method before the merging of additional satellite data into the final L4 product.

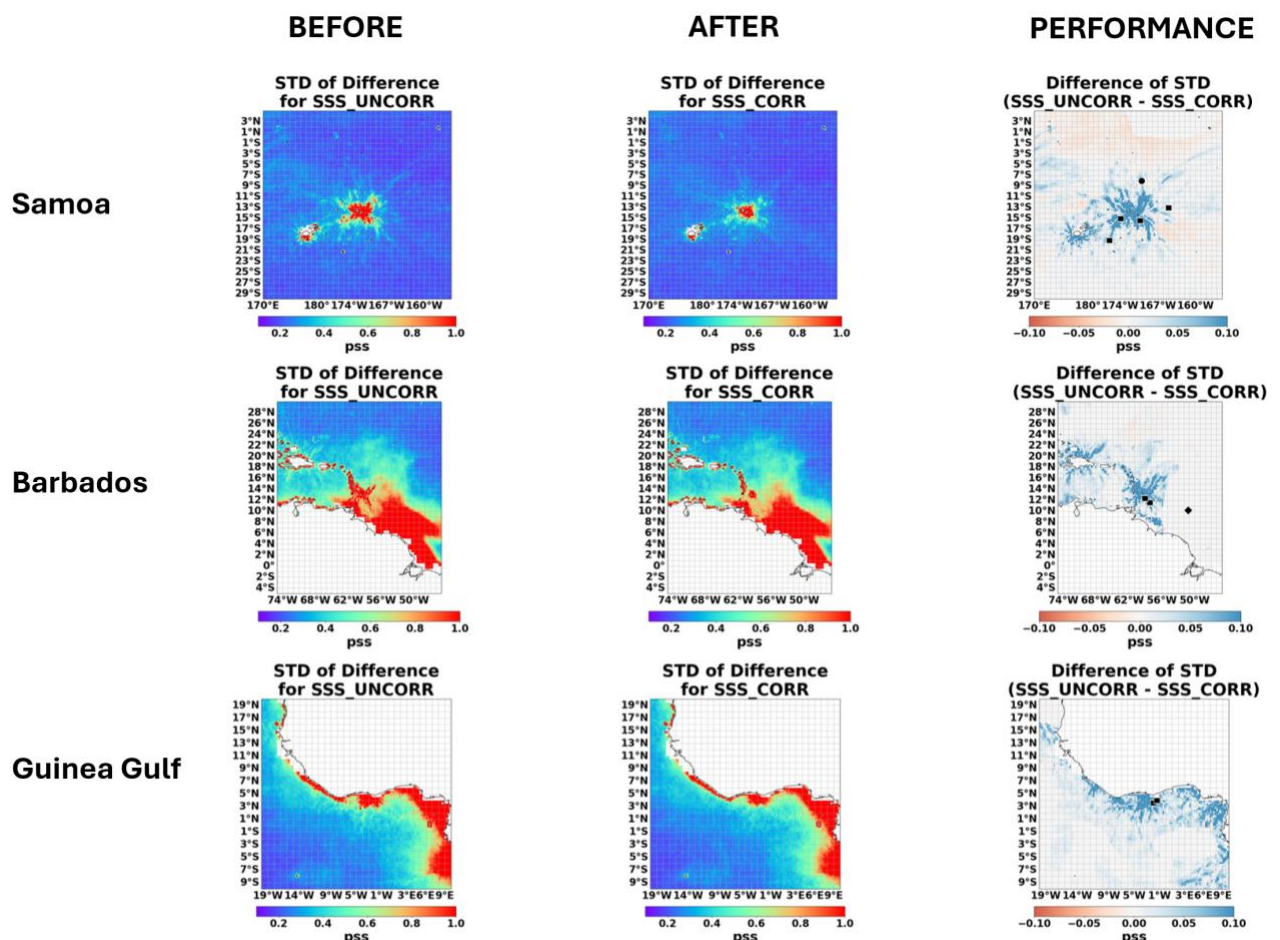


Figure 23: Left and Center Columns: Std of the difference between gridded SMOS and ISAS20 datasets before and after RFI correction, $std(SMOS - ISAS)$. Right Column: Difference between the maps in the left and center columns, $std(SMOS \text{ before correction} - ISAS) - std(SMOS \text{ after correction} - ISAS)$, representing a performance metric. Positive values (blue) indicate

improvement, while negative values (red) indicate degradation. Each row corresponds to a specific region: Top – Samoa, Middle – Barbados, Bottom – Guinea Gulf.

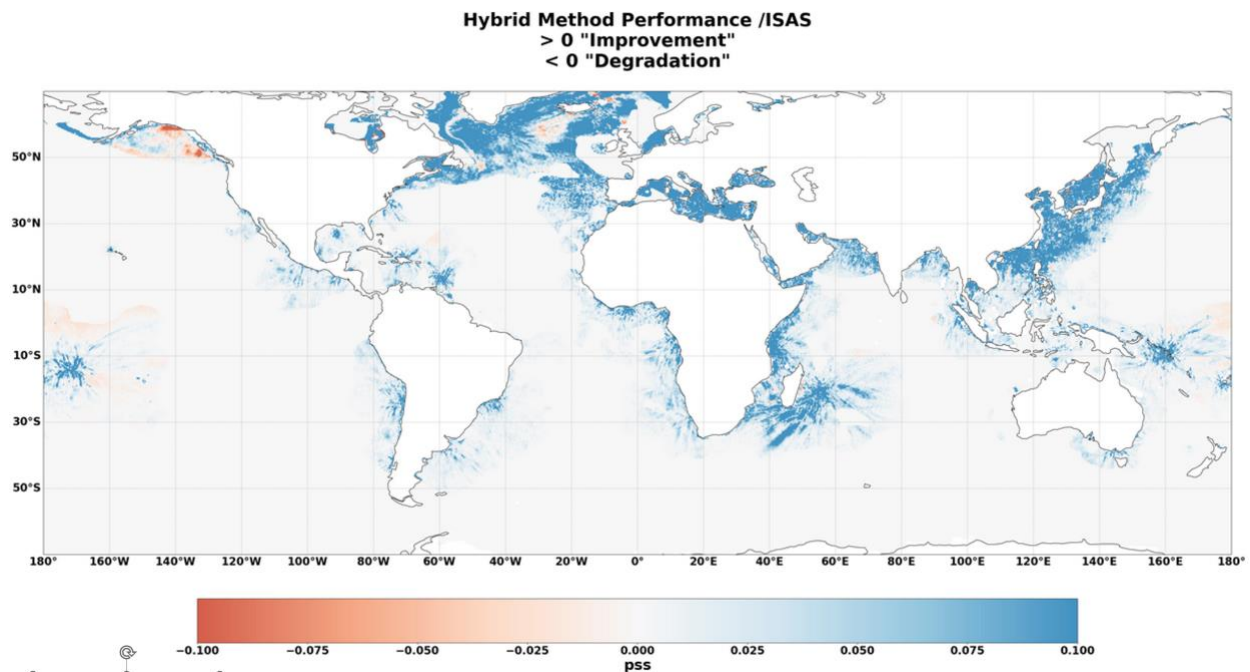


Figure 24: Same as the right column of Figure 23, but applied to the entire ocean domain, from 70°S to 70°N.

The global application of the hybrid method shows significant improvement in many areas heavily impacted by RFI contamination (Figure 19), beyond the three previously highlighted regions (Samoa, Barbados, and the Guinea Gulf). Notable improvements are observed in the China Sea, the northeastern Pacific, around Greenland and the North Pole, the Mediterranean and Black Seas, around Madagascar and La Reunion Island, and near the Solomon Islands.

However, some areas exhibit slight degradation due to the correction method, such as the Gulf of Alaska, the west coast of Canada, and a minor area north of the Samoa Islands, where, nevertheless, as noted earlier, overall improvement remains strong.

As before, these results are based solely on SMOS data, reflecting the expected performance of the hybrid method prior to the integration of other satellite datasets into the final L4 product.

4.3.3.2.3 flagging the data

We chose to apply the SSS filtering before merging and before correcting for relative and absolute biases so that to remove most of the pixels with SSS outside the reasonable oceanographic range, contaminated by ice or by RFI, or contaminated by high wind speed:

- SSS associated with wind speed larger than 16 m/s has been removed.



- SSS associated to pseudo-dielectric constant (A_{card}) is kept only if $|A_{card}^{smos} - A_{card}^{mod}| < 2$ and $A_{card} > 42$. This filtering allows removing part of the ice and of the RFI contamination.
- SSS is kept if $SSS > 2$ & $SSS < 45$
- SSS is removed if $\chi > 3$ or SSS random uncertainty > 3 .
- SSS is removed if the acquisition occurs too far from the center of the track: $abs(x_{swath}) > 400\text{km}$.
- SSS is kept if $fg_outlier = 0$ ($fg_outlier$ is raised at L2OS if the number of TB outlier data is lower than a given threshold).

4.3.3.3 SMAP L2 data

For CCIv5, we used SMAP L2C v5.3 products (SMAP_RSS_L2_SSS_V5.3, RD18), SSS at 40 km resolution.

The main differences between v5.0 and v5.3 are described in RD18. Following changes and corrections have been performed:

- RFI filtering
- salty salinity biases near the continental shelf during the early months of the SMAP mission have been corrected
- small SSS biases depending on the SMAP look direction have been corrected
- salty biases at high northern latitudes have been corrected
- small revision to the flagging for sun-glint has been made

4.3.3.4 Random uncertainty

An empirical estimation is performed for the SSS L2 uncertainty estimate (see [AD 06]) by using self-consistency approach. For SMAP, it is possible to compare SSS coming from aft and fore acquisition and to compute the std of the difference which should be an estimator of the SSS random uncertainty multiplied by $\sqrt{2}$ (assuming that the random uncertainty according to SST is the same for aft and for acquisition). This yields the relationship of the SSS uncertainty according to the SST (Figure 25). This uncertainty is derived far from coast to avoid land and RFI contamination effects. This empirical uncertainty is not used during the L4 optimal analysis (L2C theoretical random uncertainty is used).

As for SMOS, specific processing is implemented by multiplying the previous random uncertainty by a factor depending on the distance to the coast $f(\text{dist})$ (Figure 26). This factor

was obtained by comparing the open ocean uncertainty with an error estimation according to the coast distance. Indeed, coast contaminations are expected due to secondary lobe and RFI.

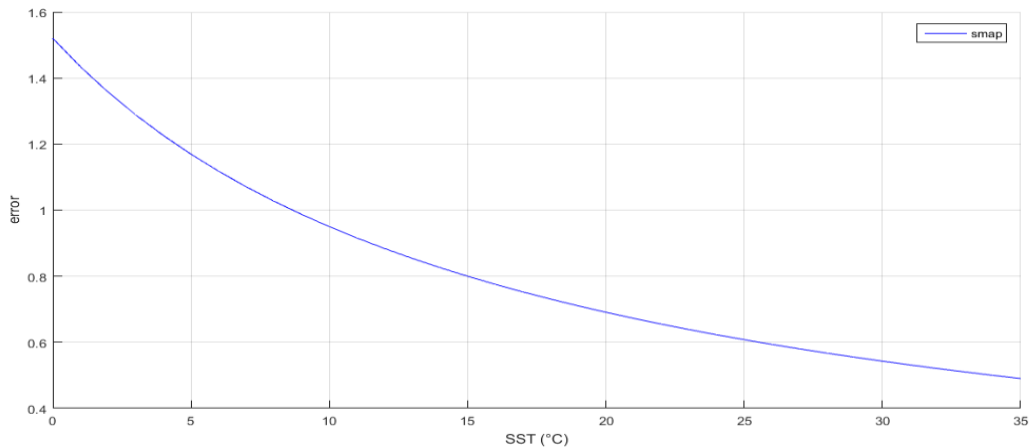


Figure 25: SSS SMAP uncertainty obtained by comparing aft and fore acquisitions.

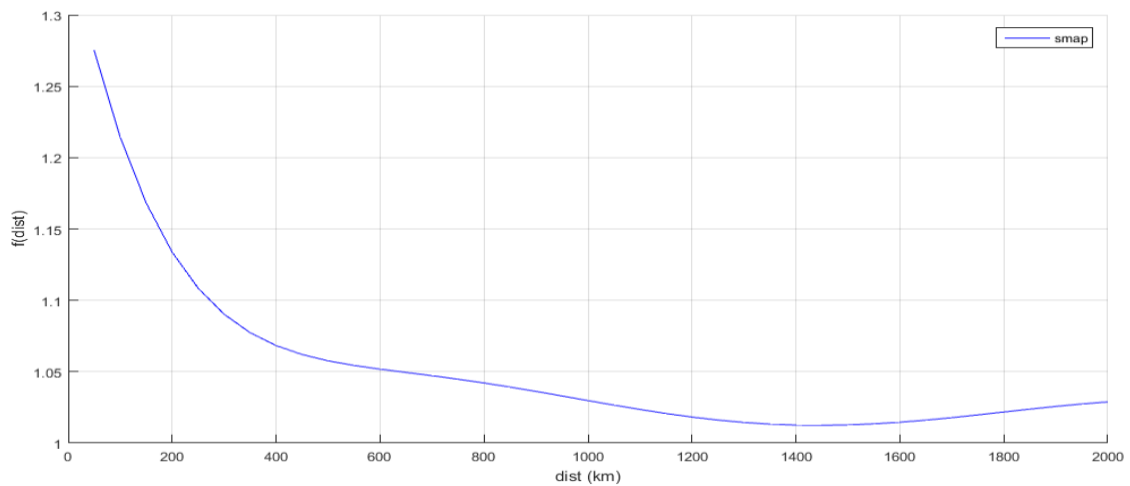


Figure 26: uncertainty factor according to the distance to the coast. SMAP.

4.3.3.4.1 Systematic uncertainty

4.3.3.4.1.1 Characterization of systematic uncertainties related to the dielectric constant

The dielectric constant model used in the SMAP processing is that of Meissner & Wentz. The impact of model differences (Klein & Swift, BV, BVZ) on the SSS plays out mainly at low SST. Moreover, the biases at low SST are much less critical on SMAP than on SMOS. We proceeded to a systematic correction in this situation according to the SST. This correction is empirical and uses ISAS as a reference. This correction is shown in Figure 27. It is very similar for ascending

and descending orbits except at very low SST, where a discrepancy occurs because of the need for more data.

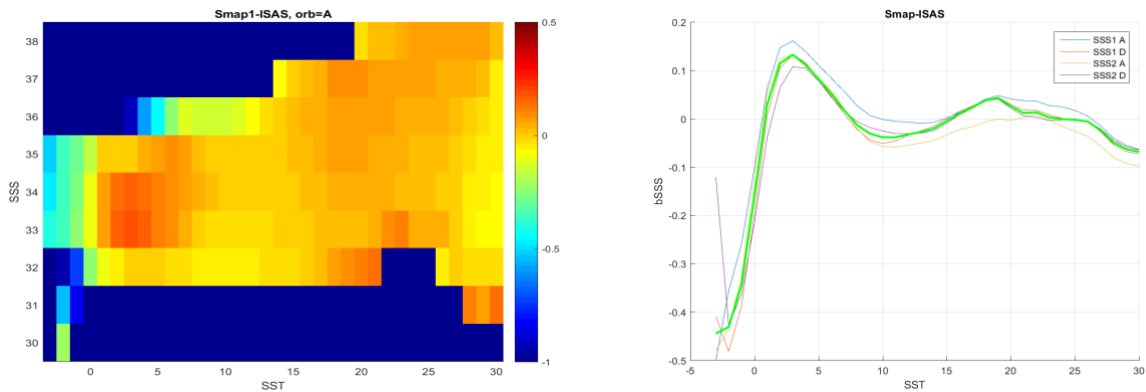


Figure 27. Left: SSS bias in the (SSS,SST) plan. Fore acquisition, A orbits. Right: average bias according to SST. In green, the average relation for the corrections. SMAP.

4.3.3.4.1.2 Characterisation of latitudinal seasonal systematic uncertainties

In order to correct for latitudinal biases, we do not apply any particular mask. The pixels contaminated by land have been filtered out (see 4.3.3.4.2). The latitudinal biases are characterized by orbit type (ascending or descending) and acquisition direction (aft and fore).

Once the correction has been applied, a check on the effect of the correction is required, in particular, to identify inter-annual biases that could not be corrected.

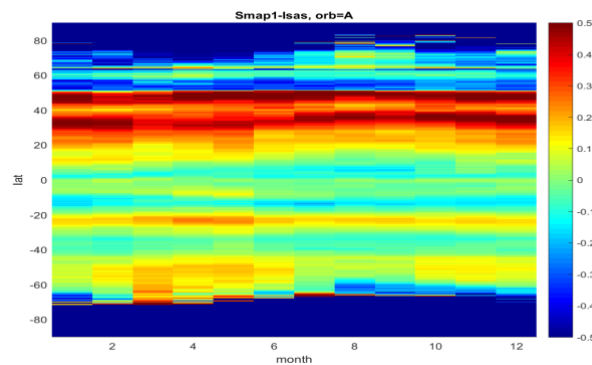


Figure 28: Seasonal latitudinal correction for SMAP. Fore acquisition, ascending orbits.

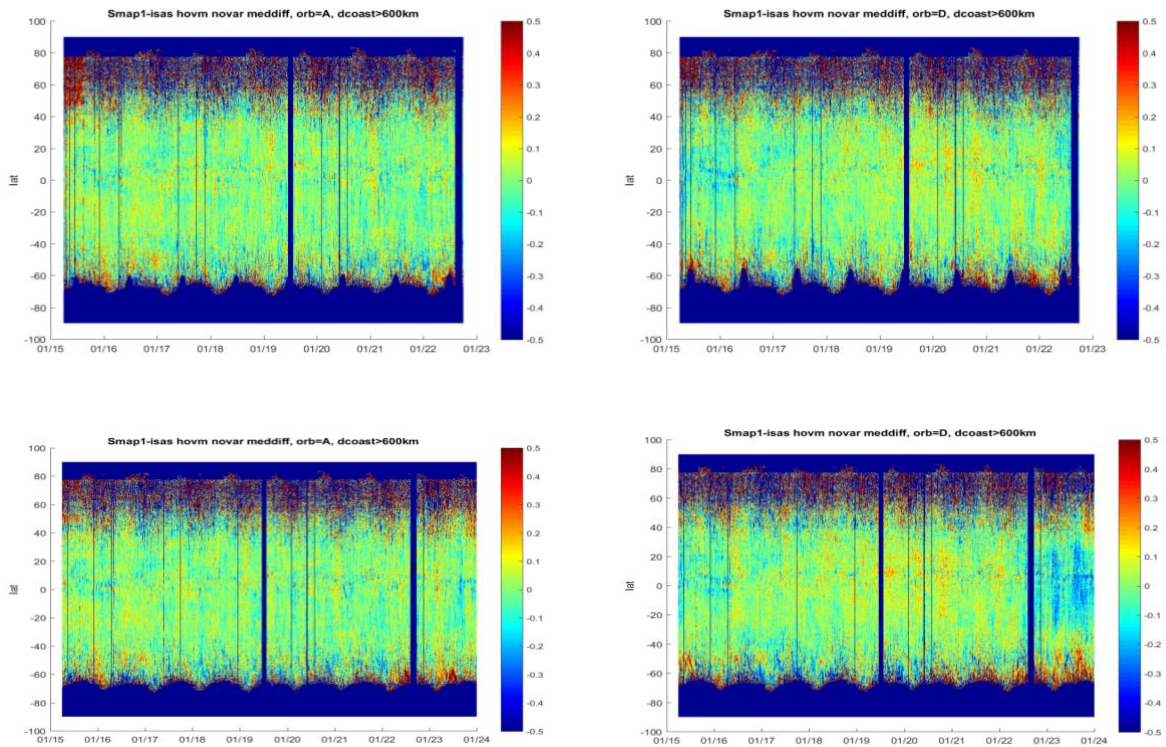


Figure 29: SMAP-1SAS after SST and latitudinal fore acquisition correction. Left: ascending orbits; right: descending orbits. Uncorrected inter-annual biases are observed in descending orbits, from beginning of 2013. Top: SMAPv5.0; bottom: SMAPv5.3.

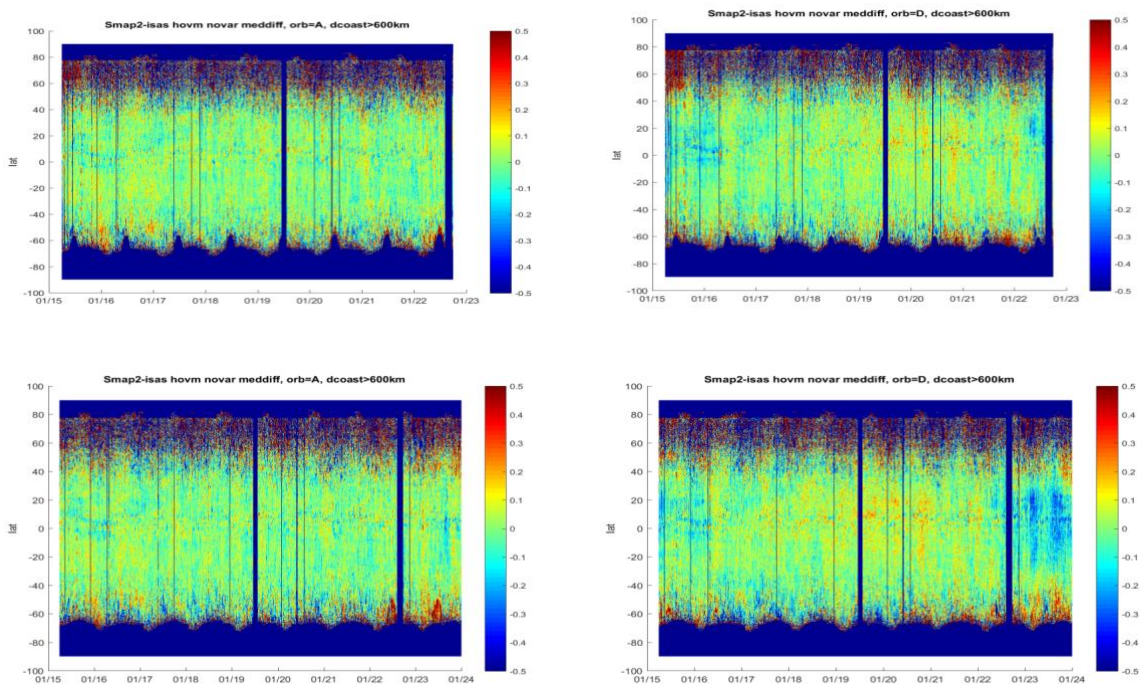


Figure 30: idem Figure 29 for afte acquisition.



4.3.3.4.2 flagging the data

We describe below the flags we apply on the SMAP L2 SSS at 40 km. We use analogous filtering as the one used by RSS team. We exclude all the SSS at 40 km which have not been included for the 70-km smoothed product :

- The sun glint angle is less than 50°, and the azimuthal look angle lies between 30° and 50° (bit 5 in L2 Q/C flag is set).
- The moon glint angle is less than 15° (bit 6 in L2 Q/C flag is set).
- The v/h-pol average of the reflected galactic radiation exceeds 2.0 K (bit 7 in L2 Q/C flag is set).
- moderate land contamination: gain weighted land fraction gland exceeds 0.04 or land fraction in 3-dB footprint fland exceeds 0.005 (bit 8 in L2 Q/C flag is set)
- moderate sea ice contamination (bit 9 in L2 Q/C flag is set)
- TB consistency, defined as the $\sqrt{\chi^2}$ of the MLE in the salinity retrieval algorithm, exceeds 1.0 K (bit 10 in the L2 Q/C flag is set).
- WS<15m/s
- SSS removal is associated with an instantaneous rain rate larger than 0.5 mm/h (no correction applied for SMOS).

4.3.3.5 Aquarius L3 data

The following dataset is used for CCIv5: RSS L3 v5, ascending and descending separated products. The same product was used for CCIv4.

4.3.3.6 Random uncertainty

The random uncertainties can be calculated by comparing the SSS at time t with the SSS at time t+7 days due to the 7-day periodicity of the satellite orbit. SSS on the open ocean is assumed to stay mostly the same in 7 days. The standard deviation of the difference then gives a fairly precise idea of the random uncertainties (multiplied by sqrt (2)). Figure 31 shows the standard deviation as a function of SST obtained far from coast.

As for SMOS and SMAP, specific processing is implemented by multiplying the previous empirical uncertainty (obtained far from the coast) by a factor depending on the distance to the coast f(dist) (Figure 32). This factor was obtained by comparing the open ocean uncertainty with an error estimation according to the coast distance. Indeed, coast contaminations are expected due to secondary lobe and RFI.

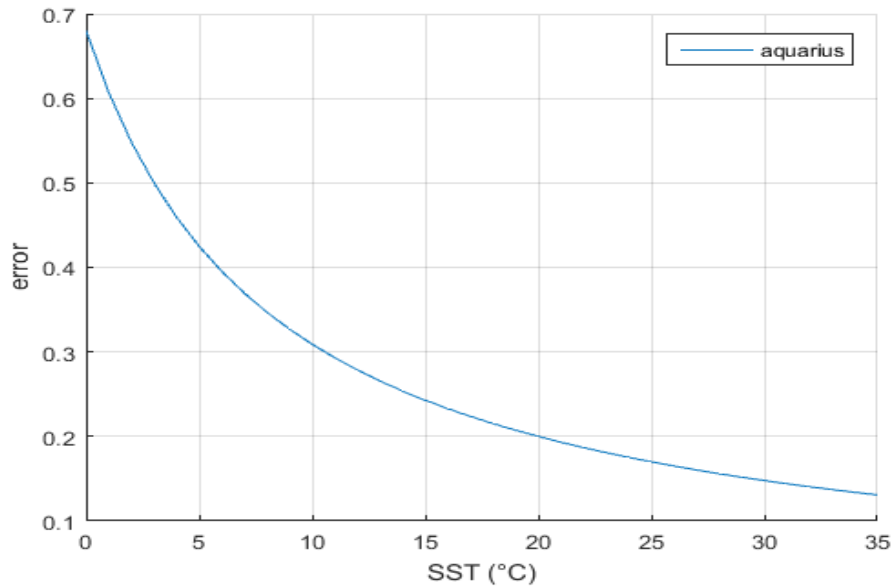


Figure 31: SSS Aquarius uncertainty obtained by comparing 7 day acquisitions.

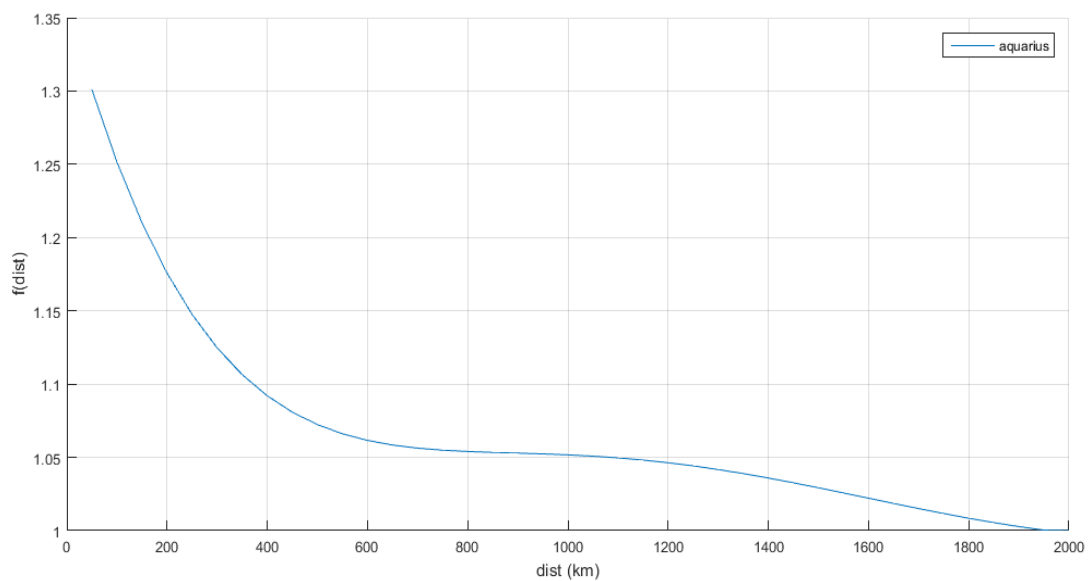


Figure 32: uncertainty factor according to the distance to the coast. Aquarius.

4.3.3.7 Systematic uncertainty

4.3.3.7.1.1 Characterisation of systematic uncertainties related to the dielectric constant

An error in the dielectric constant model has an effect expected to depend on the SST. For this reason, we sought to characterize the bias in SSS as a function of SST. In the southern Indian Ocean, we observe a positive anomaly that seems to be correlated with the SST front (Figure 33). In the (SSS SST) plan, the SSS bias follows a law essentially driven by the SST (Figure 34).

Finally, when plotting the bias as a function of SST, the ascending and descending orbits provide the same trend with an overestimation of the Aquarius SSS at low SSTs and a slight underestimation of the SSS around 5°C (Figure 34). Based on these results, an SST-dependent correction was applied (green curve in Figure 34).

The effect of this correction on the Aquarius-ISAS hovmöller and SSS maps averaged over two years (2013 and 2014) is shown in Figure 35. It can be seen that the strong biases are very much attenuated after correction. However, this does not remove all the latitudinal seasonal biases.

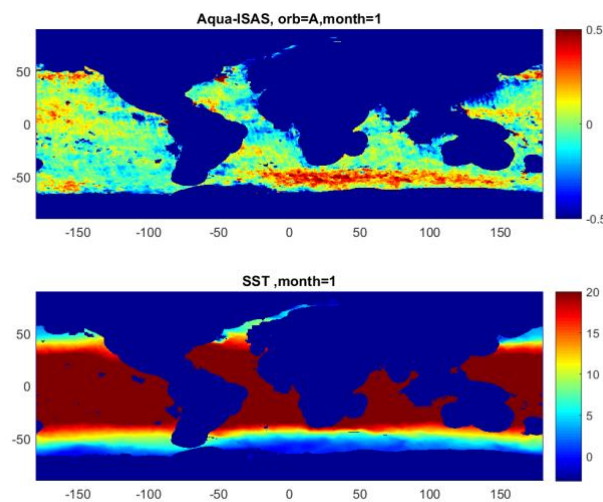


Figure 33: Example of the Aquarius bias for January (climatology) to be compared with the SST field. The positive SSS anomaly in the Southeastern Atlantic Ocean and Indian Ocean is correlated with a northern SST front.

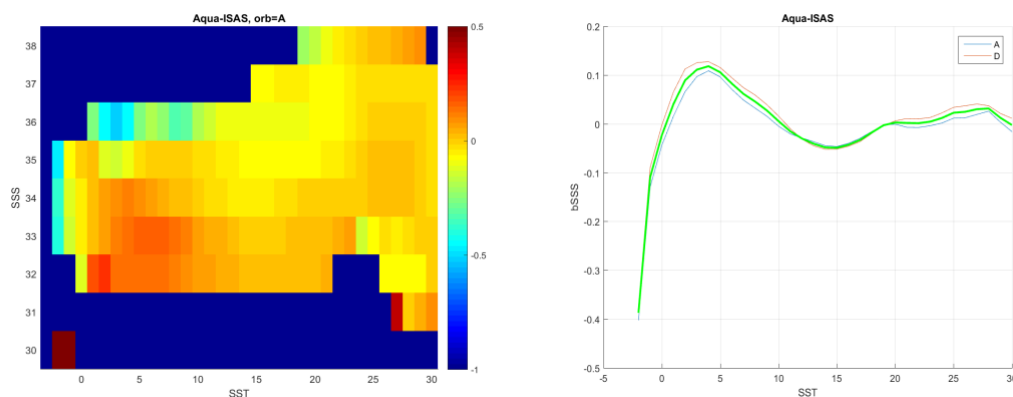


Figure 34. Left: Aquarius bias in the (SSS,SST) plan. Right: bias as a function of SST. In green, the average relationship for the corrections; in blue, the relationship obtained with ascending orbits and in red, with descending orbits.

There is a small dependence of the bias on SSS, which we did not consider.

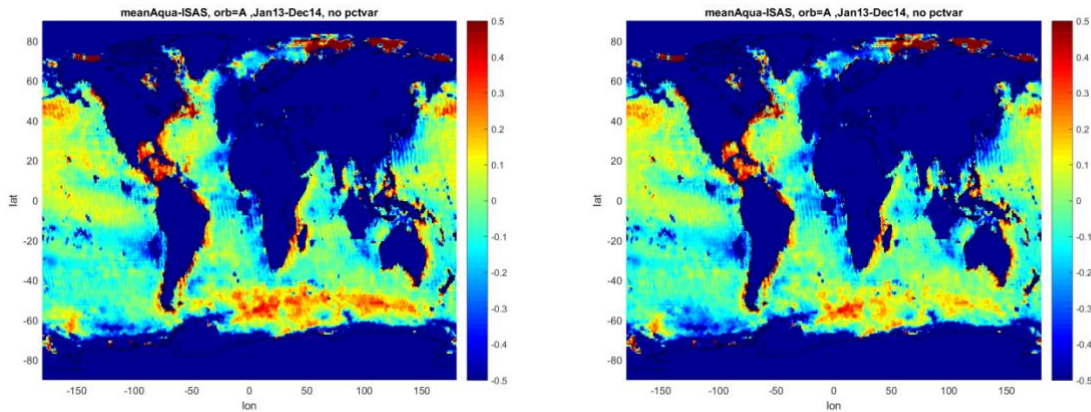


Figure 35: Aquarius-ISAS differences over 2013-2014. Left, uncorrected for SST; right, corrected for SST. Ascending orbits.

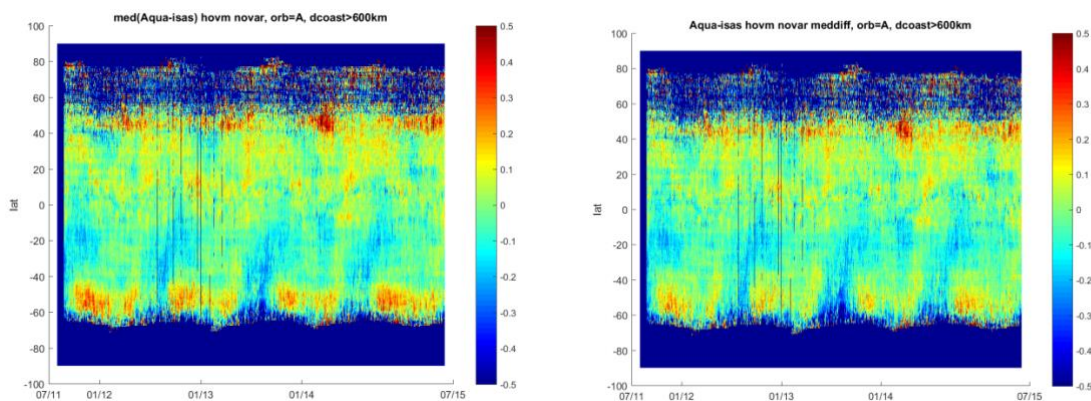


Figure 36: Hovmöller of the Aquarius-ISAS difference. Left, uncorrected for SST; right, corrected for SST. Ascending orbits.

4.3.3.7.1.2 Characterisation of latitudinal seasonal systematic uncertainties.

During phase 1 of the CCI+SSS project, we observe that latitudinal biases on L4 SSS appeared at high latitudes. These biases observed up to CCI+SSS V3.2 products originate partly from Aquarius, especially at high southern latitudes. After correcting for a bias related to the SST, non-zero Aquarius - ISAS residuals still show a latitudinal seasonal signature. To estimate the correction for these latitudinal biases, we apply a 600km mask. The latitudinal biases are characterized by orbit type (ascending or descending).

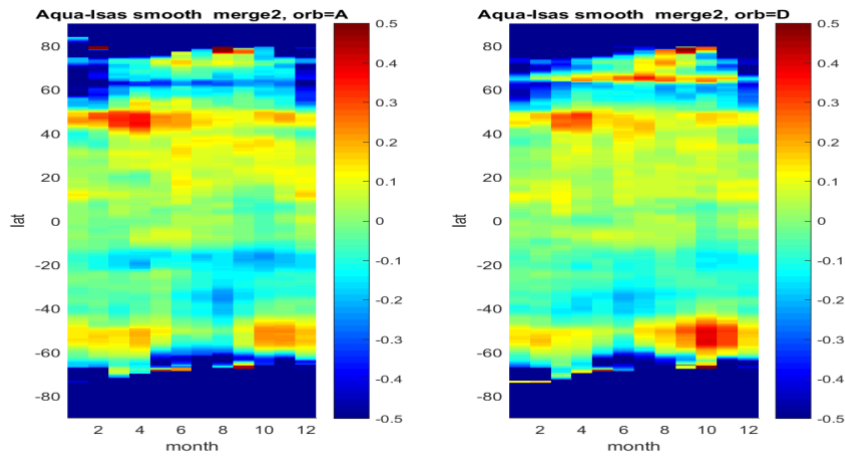


Figure 37: Latitudinal correction applied for Aquarius as a function of month and latitude. This correction is given at an average SST. Left, ascending orbits, right, descending orbits.

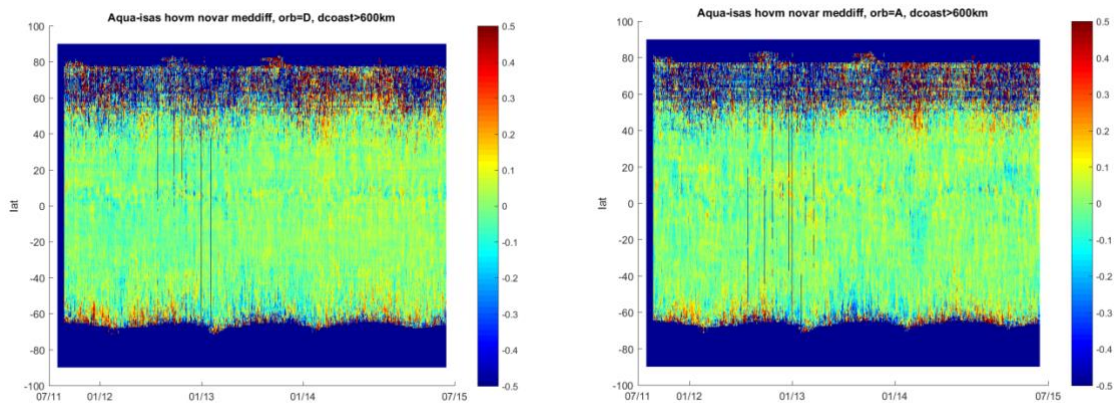


Figure 38: Hovmöller of SSS Aquarius - SSS ISAS. SSS Aquarius corrected for SST-dependent bias and latitudinal seasonal bias. Left, ascending orbits; right, descending orbits.

4.3.3.7.2 flagging the data

Aquarius L3 products are already filtered. No extra filtering is applied before merging.



5 L3 and L4 uncertainty budget

Main CCI products are L4 SSS products estimated at a weekly and a monthly resolution (with a daily and 15-day sampling, respectively). In these products, uncertainty estimation is performed using a classical least square uncertainty budget. The L2 SSS input random uncertainties are presented in this document's first part for SMOS, SMAP and Aquarius sensors. The relative systematic uncertainties are estimated simultaneously with the monthly SSS L4 estimation. The SMOS, SMAP and Aquarius latitudinal systematic uncertainties are corrected before the L4 merging.

Using L3 data allows for comparing global maps for different months and orbit types. The project provides specific L3 data with corrected and uncorrected SSS. These data are used by the validation team which is in charge the product assessment.



6 Conclusions and the way forward

Phase 2 CCI+ SSS project is dedicated to SMOS-SMAP-AQUARIUS synergy. The merging of different products from different sensors (radiometer for SMAP and AQUARIUS, interferometer for SMOS) shall consider a realistic random and systematic uncertainty model.

The self-consistency between satellite SSS measured by the various sensors and under various geometries has been used for correcting and/or estimating systematic and random uncertainties.

Due to remaining seasonal biases in CCI+SSS phase 1 products, systematic latitudinal uncertainties have been estimated for SMOS, SMAP and Aquarius at the beginning of phase 2 (in phase 1, only SMOS seasonal latitudinal biases have been corrected). Part of the seasonal biases has been removed but some inter-annual residuals remain. This interannual effect will be corrected in the next release.

Specific RFI correction algorithms using PCA have been implemented and tested in CCIv4. This kind of correction allows taking into account the time variation of the RFI intensity. It has been generalised in the CCIv5.



***Climate Change Initiative+ (CCI+)
Phase 2***

End-to-End ECV Uncertainty Budget

Ref.: ESA-EOP-SC-AMT-2021-26

Date: 15/11/2024

Version: v5.0

Page: 67 of 67

End of document